

CERTIFIED VS. EMPIRICAL ADVERSARIAL ROBUSTNESS VIA HYBRID CONVOLUTIONS WITH ATTENTION STOCHASTICITY

Joy Dhar¹, Song Xia^{*2}, Manish Kumar Pandey^{*3}, Maryam Haghighat⁴, Azadeh Alavi⁵, Ferdous Sohel⁶, Wenyu Zhang[†], Nayyar Zaidi⁷

¹Indian Institute of Technology Ropar ²Nanyang Technological University ³RoentGen Health
⁴Queensland University of Technology ⁵RMIT University ⁶Murdoch University ⁷Deakin University

ABSTRACT

We introduce *Hybrid Convolutions with Attention Stochasticity* (HyCAS), an adversarial defense that narrows the long-standing gap between *provable* robustness under ℓ_2 certificates and *empirical* robustness against strong ℓ_∞ attacks, while preserving strong generalization across *diverse imaging benchmarks*. HyCAS unifies deterministic and randomized principles by coupling 1-Lipschitz, spectrally normalized convolutions with two stochastic components—*spectral normalized random-projection filters* and a *randomized attention-noise mechanism*—to realize a *randomized defense*. Injecting smoothing randomness *inside* the architecture yields an overall ≤ 2 -Lipschitz network with formal certificates. Extensive experiments on diverse imaging benchmarks—including CIFAR-10/100, ImageNet-1k, NIH Chest X-ray, HAM10000—show that HyCAS surpasses prior leading certified and empirical defenses, boosting certified accuracy by up to $\approx 7.3\%$ (on NIH Chest X-ray) and empirical robustness by up to $\approx 3.1\%$ (on HAM10000), without sacrificing clean accuracy. These results show that a *randomized Lipschitz constrained architecture can simultaneously prove* both certified ℓ_2 and empirical ℓ_∞ adversarial robustness, thereby supporting safer deployment of deep models in high-stakes applications. **Code:** <https://github.com/mistil203/HyCAS>

1 INTRODUCTION

Despite their impressive accuracy, deep learning architectures in computer vision remain vulnerable to adversarial attacks. Such vulnerabilities threaten safety-critical deployments in fraud detection (Pumsirirat & Liu, 2018), autonomous driving (Cao et al., 2021), and clinical decision support (Dhar et al., 2025), where mistakes carry high costs. In response to these adversarial vulnerabilities, early research focused on *empirical* defences, most notably adversarial training (Madry et al., 2018; Dhar et al., 2025; Ding et al., 2019; Shafahi et al., 2019; Sriramanan et al., 2021; Cheng et al., 2023; Dhar et al., 2026). However, these methods are frequently broken by intricately crafted adversarial attacks (Carlini & Wagner, 2017; Yuan et al., 2021; Hendrycks et al., 2021; Duan et al., 2021; Li et al., 2023). This limitation has fuelled interests in *certified* robustness techniques, which offer provable guarantees that a classifier’s prediction cannot change within a specified perturbation radius (Raghunathan et al., 2018; Wong & Kolter, 2018; Hao et al., 2022).

Randomized Smoothing (RS) (Lécuyer et al., 2019; Cohen et al., 2019) certifies robustness by averaging a model’s predictions over noise-perturbed inputs at inference, and therefore scales to modern deep architectures. Yet RS is inherently rigid: large noise budgets erode clean accuracy, whereas small budgets certify only narrow ℓ_2 radii. Recent baselines seek to bypass this trade-off with *test-time* adaptations—both generic (Croce et al., 2022) and RS-specific (Alfarra et al., 2022b; Súkeník et al., 2022; Hong et al., 2022). These defences, however, are mostly heuristic-based and they quickly succumb to stronger, tailored attacks (Croce et al., 2022; Alfarra et al., 2022a; Hong et al., 2022), rekindling the familiar “cat-and-mouse” cycle of empirical defences (Athalye et al., 2018;

*Equal contribution; † Independent researcher.

Tramèr et al., 2020). Moreover, they are rarely benchmarked against state-of-the-art empirical attacks—such as APGD (Croce & Hein, 2020) or AutoAttack (Croce & Hein, 2020)—or on domain-specific distributions, such as medical-imaging datasets, thereby leaving their real-world efficacy uncertain. We move beyond pure test-time fixes and inject *fresh, independently drawn noise during both training and inference*. This two-phase strategy (i) preserves RS’s formal guarantees, (ii) alleviates the accuracy–robustness trade-off, and (iii) is validated against both certified and strong empirical attacks across *diverse imaging benchmarks*¹.

To bridge the gap between certified and empirical defenses, we introduce **Hybrid Convolution with Attention Stochasticity (HyCAS)**. HyCAS offers provable ℓ_2 adversarial robustness, boosts empirical adversarial resilience to strong ℓ_∞ attacks, and generalizes across *eight diverse vision benchmarks*. *It is a randomized defense whose architecture combines a deterministic Lipschitz-constrained design—implemented via spectrally normalized convolutions—with two stochastic smoothing modules: (i) spectrally normalized random-projection filters and (ii) randomized attention-noise injection*. These components inject controlled smoothing noise, thereby incorporating stochasticity into the architecture and yielding an overall ≤ 2 -Lipschitz network that admits formal certification while consistently enhancing empirical robustness to strong ℓ_∞ attacks.

The key contributions of this paper can be summarized as follows:

1. **Hybrid defense.** We introduce HyCAS, *a randomized Lipschitz-constrained defense that provides both certified ℓ_2 guarantees and strong empirical ℓ_∞ robustness across diverse vision benchmarks*.
2. **Theoretical guarantees.** We derive a tight ℓ_2 robustness certificate for HyCAS and show that it remains competitive in empirical adversarial robustness against state-of-the-art ℓ_∞ attacks.
3. **Plug-and-play design.** HyCAS integrates a 1-Lipschitz deterministic core—implemented via spectrally normalized convolutions—with two stochastic modules: spectral normalized random-projection filters and randomized attention noise injection. These components inject controlled smoothing noise, thereby incorporating refined stochasticity into the network. Together they form a ≤ 2 -Lipschitz network that admits formal certification while boosting empirical robustness.
4. **Comprehensive evaluation.** Experiments on several benchmarks confirm that HyCAS outperforms prior certified and empirical defenses while allowing controllable trade-offs between certificate and empirical adversarial robustness.

2 RELATED WORK

Deterministic certified defences. Bounding a network’s global Lipschitz constant makes its predictions provably stable to small ℓ_2 perturbations. Early studies constrain fully-connected layers via spectral normalisation or orthogonal parameterisations (Miyato et al., 2018). Layer-wise Orthogonal Training (LOT) (Xu et al., 2022) and the Spectral-Lipschitz Lattice (SLL) (Araujo et al., 2023) extend these ideas to CNNs, yet often sacrifice clean accuracy on high-resolution data. Our deterministic backbone inherits its 1-Lipschitz guarantee while compensating for the accuracy drop through stochastic branches.

Stochastic certified defences. Randomised smoothing (RS) converts any base classifier into a Gaussian ensemble whose majority vote is certifiably robust (Cohen et al., 2019). Subsequent work enlarges certificates via adversarially trained bases (Salman et al., 2019), consistency regularisation (Jeong & Shin, 2020), and noise-aware denoising (Carlini et al., 2023). Mixing multiple noise scales further tightens guarantees, as shown by Dual RS (DRS) (Xia et al., 2024), Incremental RS (IRS) (Ugare et al.), and Adaptive RS (ARS) (Lyu et al., 2024). Our HyCAS departs from pure input-noise smoothing by injecting *internal* randomness via dual stochastic noise—yet still preserves a global ≤ 2 -Lipschitz certificate.

Empirical defences. Empirical methods drop certificates to maximise robustness against high-budget ℓ_∞ attacks. PNI (He et al., 2019) learns layer-wise Gaussian noise during adversarial training, boosting both clean and robust accuracy. Learn2Perturb (Jeddi et al., 2020) generalises this idea by jointly optimising feature-perturbation modules in an EM-like loop. CTRW (Ma et al., 2023) resamples convolution kernels at inference under learned mean–variance constraints, while RPF (Dong & Xu, 2023) freezes part of the first convolution layer as Gaussian projections, both outperforming strong PGD-trained baselines. In contrast, CAP (Xiang et al., 2023) infuses lung-

¹In our experiments, we use natural vision and medical imaging datasets *as diverse imaging benchmarks*.

edge priors, bolstering adversarial robustness in COVID-19 CT prediction. *Despite these gains, these empirical defences provide no certified worst case guarantees (Yang et al., 2022; Liu et al., 2021), and many rely on input independent randomization (He et al., 2019; Jeddi et al., 2020; Dong & Xu, 2023); these non-certified randomized defences have often been circumvented by adaptive attacks that explicitly average over the internal noise (Athalye et al., 2018; Tramèr et al., 2020).*

Most prior defenses optimize for *either* certified *or* empirical robustness and are validated on a single regime—usually natural images, with only a few addressing specialised medical data. *HyCAS bridges this gap by incorporating a deterministic 1-Lipschitz architecture with stochastic smoothing modules (e.g., random-projection and attention-noise mechanisms), thereby forming a randomized defense that robustly generalizes across diverse imaging benchmarks.* A modest reduction in clean accuracy yields simultaneous performance gains in certified ℓ_2 and empirical ℓ_∞ robustness (Fig. 4). Consequently, HyCAS aims to surpass the strongest deterministic certifiers *and* the leading empirical defences. Further details appear in Appendix A.1 (related work) and Appendix A.2 (preliminaries).

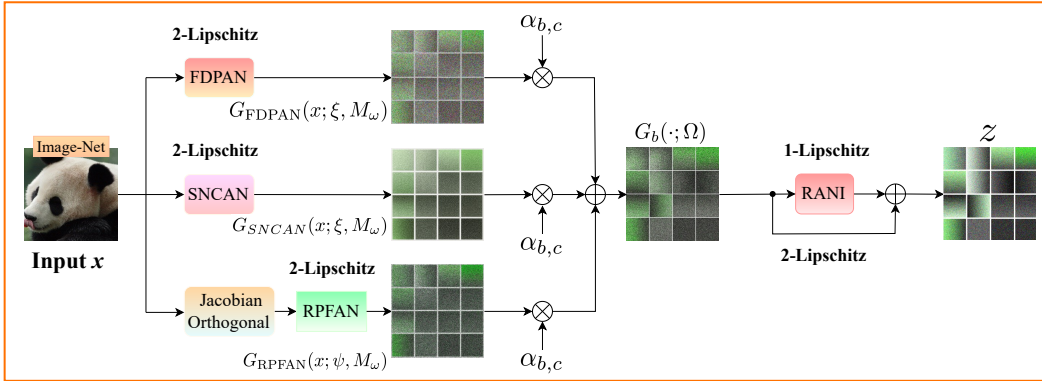


Figure 1: Overview of HyCAS mechanism. It consists of three parallel streams—FDPAN, SNCAN, and RPFAN—each built from 1-Lipschitz cores with Randomized Attention Noise Injection (RANI) residuals. Per-channel convex gating fuses the streams to form $G_b(\cdot; \Omega)$. Each stream is ≤ 2 -Lipschitz; the fused stream and the stacked network remain ≤ 2 -Lipschitz, enabling a margin-based ℓ_2 certificate.

3 HYBRID CONVOLUTIONS WITH ATTENTION STOCHASTICITY

Randomized defenses often incorporate stochasticity into deep network structures by (i) tuning data-dependent hyper-parameters (e.g. noise scale, sampling rate) or (ii) *data-independent* architectural modifications. However, deep networks remain highly vulnerable on vision benchmarks, where imperceptible perturbations can sharply degrade accuracy. *Randomization alone is often insufficient; coupling it with a Lipschitz-constrained deterministic architecture yields stronger certified and empirical robustness.*

To address these limitations, we propose **Hybrid Convolution with Attention Stochasticity (HyCAS)**, which replaces each convolutional layer in standard CNN backbones with Lipschitz-bounded stochastic streams that inject refined smoothing and controlled randomness into the network via two complementary, data-independent components—(i) a *Lipschitz-constrained deterministic architecture* and (ii) a *dual stochastic design*—thereby improving adversarial robustness.

Let $x \in \mathbb{R}^{H \times W \times C}$ be an input feature map with spatial dimensions (H, W) and C channels with label $y \in \mathcal{Y} = \{1, \dots, K\}$. We denote by $\|\cdot\|_2$ the Euclidean norm over vectorized tensors and by $\text{Lip}(h)$ the (global) ℓ_2 -Lipschitz constant of a map h (“ L -Lipschitz” means $\|h(u) - h(v)\|_2 \leq L\|u - v\|_2$). Our proposed HyCAS—integrated any base classifier f_θ with parameters θ . The smoothed classifier induced by HyCAS is:

$$g_\theta(x) = \arg \max_{c \in \mathcal{Y}} \mathbb{P}_{\varepsilon, \Omega} [f_\theta(x + \varepsilon; \Omega) = c]. \quad (1)$$

where $\Omega = (\xi, \psi, M_\omega)$, $\varepsilon \sim \mathcal{N}(0, \sigma^2 I)$ denotes Gaussian noise with mean 0 and standard deviation σ matching the dimensions of x to enable randomized smoothing, ξ induces *deterministic Lipschitz-constrained structure*, ψ integrates *implicit structural randomness* (first-level stochastic defense), and M_ω injects the *explicit attention noise* (second-level stochastic defense). The classifier $g_\theta(\cdot)$

returns whichever class f_θ is most likely to return, taking expectations over the distributions $\mathcal{N}(x + \varepsilon; x, \sigma^2 I)$. An overview is given in Fig. 1; *pseudocode is provided in App. A.7-A.8 (Algorithms 1–3)*.

HyCAS processes every feature map through three parallel streams: (a) *Frequency-aware Deterministic Projection with Attention Noise* (FDPAN); (b) *Spectrally Normalized Convolution with Attention Noise* (SNCAN); and (c) *Random Projection Filter with Attention Noise* (RPFAN). Their outputs are fused by a data-independent convex channel gate that down-weights high-sensitivity streams, thereby weakening naïve adversarial attacks.

Specifically, let $\mathcal{B} = \{\text{FDPAN}, \text{RPFAN}, \text{SNCAN}\}$ be the set of streams and for each stream $b \in \mathcal{B}$, let $G_b(\cdot; \Omega)$ denote its output feature map and those output feature maps are fused by channel-wise convex gate $\alpha_{b,c}$. For learnable, data-independent logits $\lambda_{b,c}$, we define channel-wise convex weights $\alpha_{b,c} = \frac{\exp(\lambda_{b,c})}{\sum_{b' \in \mathcal{B}} \exp(\lambda_{b',c})}$, such that $\sum_b \alpha_{b,c} = 1$, $\alpha_{b,c} \geq 0$, thereby we obtain the HyCAS block output is

$$z(x)_{:,c} = \sum_{b \in \mathcal{B}} \alpha_{b,c} [G_b(x; \Omega)]_{:,c} + R \left(\sum_{b \in \mathcal{B}} \alpha_{b,c} [G_b(x; \Omega)]_{:,c}; M_\omega \right); \quad c = 1, \dots, C. \quad (2)$$

where R denotes RANI module.

Convex fusion and expected-logit map are ≤ 2 -Lipschitz. If each stream satisfies $\text{Lip}(G_b) \leq 2$, and the gate is convex (Eq. 2), then the per-channel fusion has $\text{Lip}(x \mapsto z(x)) \leq \max_{b \in \mathcal{B}} \text{Lip}(G_b) \leq 2$. (*ref. Appendix A.3 (Prop. 4)*). Taking the expectation over Ω preserves the Lipschitz constant (*ref. Appendix A.3 (Lemma 2)*), so the network’s expected logit map $Z(x) := \mathbb{E}_\Omega[s_\theta(x; \Omega)]$ remains ≤ 2 -Lipschitz. Formally:

Theorem 1 (HyCAS block is ≤ 2 -Lipschitz). *Each constituent stream—SNCAN, RPFAN, and FDPAN with skip weight $\beta \leq \frac{1}{3}$ —is individually ≤ 2 -Lipschitz. Indeed, every stream is the composition of three maps: (i) a stochastic projection \mathcal{T}_ψ (seeded by ψ), 1-Lipschitz; (ii) a deterministic projection \mathcal{D}_ξ (parameterized by ξ), 1-Lipschitz; and (iii) a stochastic attention noise $M_\omega: \mathbb{R}^d \rightarrow [0, 1]^d$, 1-Lipschitz. For any input x , the resulting feature map*

$$G_b(x; \xi, \psi, \omega) = \mathcal{D}_\xi(\mathcal{T}_\psi(x)) + M_\omega(\mathcal{D}_\xi(\mathcal{T}_\psi(x)))$$

is therefore 2-Lipschitz on each forward pass. The subsequent per-channel convex fusion is non-expansive, so it cannot increase the Lipschitz constant. Consequently, every HyCAS block is provably ≤ 2 -Lipschitz (see Appendix A.3 (Prop. 4)).

Proof. See proof within the Appendix A.3. □

Corollary 1 (*Randomized Lipschitz margin certificate for expected logits*). *Let $Z(x)$ be HyCAS logits averaged over internal randomness, with $\text{Lip}(Z) \leq 2$. Let $\Delta(x) = Z_{(1)}(x) - Z_{(2)}(x)$ is the gap between the top-two logits. Then $r_2(x) = \frac{\Delta(x)}{4}$ is a valid ℓ_2 certificate: for all $\|\delta\|_2 < r_2(x)$, we have $\arg \max Z(x + \delta) = \arg \max Z(x)$. This is the HyCAS pointwise ℓ_2 certificate (App. A.4).*

Proof. See proof within the Appendix A.3. □

The HyCAS-integrated network is optimised with a standard ℓ_2 loss as:

$$\mathcal{L}_{\text{HyCAS}} = \zeta \odot \mathcal{L}_{\text{FDPAN}} + \varphi \odot \mathcal{L}_{\text{SNCAN}} + \nu \odot \mathcal{L}_{\text{RPFAN}} + \kappa \odot \mathcal{L}_{\text{RANI}}, \quad (3)$$

where ζ, φ, ν , and κ denoted by learnable parameters, while \odot represents Hadamard product.

All streams are spectrally normalised ($\|W\|_2 \leq 1$) and the stochastic attention noise module is 1-Lipschitz. Hence, by Theorem 1–Corollary 1, every HyCAS block—and any network built by stacking them—is ≤ 2 -Lipschitz, so attacks with ℓ_2 -norm $< \Delta(x)/4$ cannot alter the prediction.

3.1 FREQUENCY-AWARE DETERMINISTIC PROJECTION WITH ATTENTION NOISE (FDPAN)

Under ℓ_2 -bounded attacks, adversaries (i) conceal perturbations in high-frequency DCT coefficients and (ii) exploit channel-wise gradient regularities that generalize across models. FDPAN counters both phenomena by weaving *frequency truncation, channel scrambling, spectral control, and calibrated stochasticity* into the architecture.

FDPAN is a four-stage cascade (*see Appendices A.3–A.5 for Lemma 3 and Figure 5*), where each component comprises a deterministic 1-Lipschitz core followed by two randomized residuals, i.e.,

Table 1: Certified accuracy (%) of HyCAS and prior baselines on CIFAR-10 and ImageNet. Bold value denotes the best in each column across all noise-radius pairs. All methods are evaluated at two noise levels.

Approaches	σ	CIFAR-10								ImageNet							
		Certified accuracy at predetermined ℓ_2 radius r (%)								Certified accuracy at predetermined ℓ_2 radius r (%)							
		0.00	0.25	0.50	0.75	1.00	1.25	1.50	2.0	0.00	0.25	0.50	0.75	1.00	1.25	1.50	2.0
RS	0.25	75.3	60.2	43.4	26.1	0	0	0	0	67.1	48.7	0	0	0	0	0	0
	0.50	65.2	54.1	41.3	32.4	23.2	14.7	9.34	0	57.3	45.9	36.8	28.7	0	0	0	0
IRS	0.25	78.6	63.2	47.5	30.8	19.6	10.3	5.72	0	68.4	58.5	46.2	38.7	32.1	19.3	10.8	0
	0.50	71.3	58.5	44.1	33.3	24.1	15.7	11.4	2.2	62.4	50.9	41.5	34.7	27.3	20.2	13.8	6.31
DRS	0.25	83.4	65.8	50.2	34.5	24.7	15.8	10.5	0	70.6	61.2	51.8	42.7	38.4	32.6	25.4	0
	0.50	78.1	62.1	48.7	35.8	24.5	17.9	12.9	4.6	67.6	58.2	49.6	42.8	35.6	33.2	29.8	21.3
ARS	0.25	84.1	67.3	51.4	39.1	30.9	21.1	16.2	0	71.1	61.4	52.7	43.1	39.1	33.4	26.7	0
	0.50	78.4	63.7	50.2	38.9	31.8	23.3	19.7	8.47	68.1	58.7	50.3	43.4	39.1	34.5	30.6	22.4
LOT	—	80.5	64.7	48.6	34.3	23.6	15.2	9.14	0	69.7	60.6	50.9	42.2	37.1	30.5	21.8	0
	—	76.7	60.4	46.3	35.1	24.9	17.3	12.1	6.25	66.1	57.4	48.9	42.8	38.4	32.9	28.3	19.8
SLL	—	81.4	65.3	49.9	33.1	23.6	14.7	9.94	0	70.2	57.7	48.4	41.8	37.6	31.9	24.3	0
	—	77.9	62.6	48.7	34.5	24.4	16.2	13.7	5.83	67.3	55.5	49.1	42.8	39.1	34.5	26.7	21.3
HyCAS	0.25	85.4	70.1	56.7	44.3	36.5	29.6	22.9	8.52	72.3	63.9	55.6	46.4	40.7	35.2	29.7	5.42
	0.50	80.7	65.3	54.8	44.3	36.8	30.3	23.4	12.5	69.2	60.6	53.9	45.6	41.1	36.3	32.7	24.8

2-Lipschitz: (i) *Low-pass DCT mask* (1-Lipschitz) — excises fragile high-frequency bands. (ii) *Orthogonal Jacobian 1×1 matrix + Randomized Attention Noise Injection (RANI)* (2-Lipschitz) — scrambles channel gradients and injects structured noise. (iii) *SNCAN* (2-Lipschitz) — keeps the convolutional kernel spectrum bounded while introducing additional stochasticity. (iv) *RANI* that further incorporates refined randomness and is 2-Lipschitz.

Let the deterministic core be $H(x) = C_{K_e} \left(U \Phi^\top (\Lambda \odot \Phi x) \right)$, where C_{K_e} be Spectrally normalized convolution, U denotes Orthogonal Jacobian matrix layer, Φ is the orthonormal 2-D DCT and Λ is the low-pass mask.

To incorporate richer, refined stochasticity, we apply RANI immediately after the deterministic core. Given an attention noise M_ω and a noise-strength parameter $\omega \in [0, 1]$, a RANI module is denoted by $R(x; M_\omega)$, and is 1-Lipschitz for every freshly drawn ω during both training and inference. Hence, combining the deterministic path and two independent RANI injections (stochastic) yields the FDPAN stream output as: $G_{\text{FDPAN}}(x; \xi, M_\omega) = H(x; \xi) + R(H(x; \xi); M_{\omega_i})$, where $H(\cdot; \xi)$ is the deterministic core, and each $R(\cdot; M_{\omega_i})$ introduces independent stochastic attention noise M_{ω_i} for $i \in \{1 : 2\}$. Because the two M_{ω_i} terms are cascaded i and the entire stream is at most 2-Lipschitz by the triangle inequality. The skip connection is 1-Lipschitz as well. *Notably, more details about SNCAN module and RANI mechanism are in the following sections.* Formally:

Proposition 1 (FDPAN is at most 2-Lipschitz). *Assume the deterministic core $H(\cdot)$ is 1-Lipschitz and that, for every attention noise M_{ω_i} , the RANI $R(\cdot; \omega_i)$ is also 1-Lipschitz; the skip connection is likewise 1-Lipschitz. Define the FDPAN stream output by $G_{\text{FDPAN}}(x; M_\omega) = H(\cdot) + (R(\cdot) \circ H(\cdot))$ is 4-Lipschitz and therefore satisfies $\text{Lipschitz}(G_{\text{FDPAN}}) \leq 2$.*

Proof. See proof within the Appendix A.3. □

Therefore, FDPAN minimises the objective of HyCAS by incorporating refined stochasticity into the network through all employed modules as mentioned in the above:

$$\mathcal{L}_{\text{FDPAN}}(\theta) = \min_{\theta} \mathbb{E}_{(x,y)} \mathbb{E}_{\varepsilon \sim \mathcal{N}(0, \sigma^2 I), \xi, M_{\omega_i}} \ell(f_{\theta}(x + \varepsilon; \xi, M_{\omega_i}), y). \quad (4)$$

3.2 SPECTRALLY NORMALIZED CONVOLUTIONS WITH ATTENTION NOISE (SNCAN)

To design SNCAN (see Appendix A.5 (Figure 6)), we replace every standard convolutional layer with a *spectrally normalized convolution* (SNC; see Appendix A.2.2). This substitution introduces controlled gradient variability while preserving the deterministic 1-Lipschitz bound on worst-case ℓ_2 perturbations. However, the resulting *stationary* gradient fields can still be exploited by adversarial attacks. To mitigate this vulnerability and further strengthen robustness, we incorporate our *data-independent* RANI module (Section 3.4) to each SNC layer, thereby injecting fine-grained stochasticity while preserving a tight Lipschitz envelope.

Let $v = C_{K_e}(x)$, $R(v; M_\omega) = D_\omega v$, where C_{K_e} is an SNC with kernel K_e rescaled to satisfy $\|K_e\|_{\text{op}} \leq 1$ and $D_\omega = \text{diag}(M_\omega)$ is a diagonal matrix formed from the attention-noise tensor $M_\omega \in [0, 1]^{H \times W \times C}$. Because every diagonal entry of D_ω lies in $[0, 1]$, we have $\|D_\omega\|_2 \leq 1$. Hence $\text{Lip}(C_{K_e}) \leq 1$, $\text{Lip}(R(\cdot; M_\omega)) \leq 1$, $\text{Lip}(I + D_\omega) \leq 2$.

RANI generates a bounded attention noise $M_\omega \in [0, 1]^{H \times W \times C}$ and forms the stochastic residual output as:

$$G_{\text{SNCAN}}(x; \xi, M_\omega) = C_{K_e}(x; \xi) + R(C_{K_e}(x; \xi); M_\omega) = (I + D_\omega) C_{K_e}(x; \xi). \quad (5)$$

By incorporating RANI into a deterministic, 1-Lipschitz convolutional block, we obtain a *randomized* defense that is provably 2-Lipschitz, as formalized below.

Proposition 2 (2-Lipschitz hybrid block). *For every input pair $x, y \in \mathbb{R}^{H \times W \times C}$ and every noise sample M_ω ,*

$$\|G_{\text{SNCAN}}(x; M_\omega) - G_{\text{SNCAN}}(y; M_\omega)\|_2 \leq 2 \|x - y\|_2.$$

Proof. See proof within the Appendix A.3. □

Each SNCAN block, therefore, multiplies the network’s global Lipschitz constant by at most 2 while injecting fresh randomness on every forward pass, synchronizing the gradient landscape that an adversary sees. Therefore, SNCAN minimizes the objective of HYCAS by incorporating refined stochasticity into the network through SNC and RANI modules:

$$\mathcal{L}_{\text{SNCAN}}(\theta) = \min_{\theta} \mathbb{E}_{(x,y)} \mathbb{E}_{\varepsilon \sim \mathcal{N}(0, \sigma^2 I), \xi, M_\omega} \ell(f_\theta(x + \varepsilon; \xi, M_\omega), y). \quad (6)$$

In summary, spectral normalization (e.g., SNC) complemented by RANI yields a randomized module built on a deterministic architecture, whose Lipschitz envelope remains tight while its gradients vary across evaluations.

3.3 RANDOM-PROJECTION CONVOLUTION WITH ATTENTION NOISE (RPFAN)

RPFAN couples a spectrally controlled random projection (1-Lipschitz) with a *data-independent* randomized attention residual (2-Lipschitz). It therefore introduces *dual* stochasticity—(i) from the random projection itself and (ii) from RANI—while keeping the stream’s Lipschitz constant at most 2. In practice, both the random projection and attention noise are freshly resampled as described in §3.5. *Network Execution*.

The RPFAN module (see Appendix A.5 (Figure 7)) inherits the Johnson–Lindenstrauss (JL) embedding guarantee of a *random-projection filter* (RPF) (Dong & Xu, 2023) (see Appendix A.2.3 for details) and extends it with three carefully chosen components: (i) two **core innovations** that render the module *certifiably* 1-Lipschitz, and (ii) the RANI module, which raises the Lipschitz constant to 2 while injecting an additional source of *data-independent* stochasticity. Combined, these elements provide *dual stochasticity*—one arising from the random projection itself and the other from RANI—thereby strengthening adversarial robustness without exceeding a 2-Lipschitz bound. The three components are summarized below.

1. **Energy-preserving channel pre-mix.** Before the random-projection filter is applied, we leverage 1×1 orthogonal Jacobian matrix as channel mixer U with $U^\top U = I$ (Horn & Johnson, 2012) to apply $x \mapsto Ux$, which equalises channel energy so that every spatial dimension enters the projection space with identical energy distribution (see Appendix A.3 (Lemma 3)).
2. **Batch-aware spectral normalisation for random projection.** The random-projection filter W_0 is sampled exactly as in (Dong & Xu, 2023) (ref. A.2.3). We then rescale it using a *per-sample*, two-step power-iteration (PI) scheme: (i) Draw $u \sim \mathcal{N}(0, 1)$ of shape $(N, \frac{H}{s}, \frac{W}{s}, C_{\text{out}})$; (ii) Update twice $v \leftarrow \frac{\text{Conv}^\top(u; W_0)}{\|\cdot\|_2}$, $u \leftarrow \frac{\text{Conv}(v; W_0)}{\|\cdot\|_2}$, *normalising each sample independently*; and (iii) compute the Rayleigh quotient (RQ), thereby to form a spectral normalized random projection filter W_{SN} as:

$$RQ = \frac{1}{N} \sum_n \langle u_n, \text{Conv}(v_n; W_0) \rangle, \quad W_{\text{SN}} = \frac{W_0}{\max(RQ, 1)}.$$

This *batch-aware* PI yields a tighter bound on $\|\text{Conv}(\cdot; W_0)\|_2$ than layer-wise PI while guaranteeing that the projection remains 1-Lipschitz (Appendix A.3).

Table 2: Certified accuracy (%) of HyCAS and prior defenses on CelebA, HAM10000, and NIH-CXR. Boldface denotes the best in each column across all noise–radius pairs. Methods are evaluated at 3 noise levels.

Approaches	σ	CelebA			HAM10000			NIH-CXR		
		ℓ_2 radius r (%)			ℓ_2 radius r (%)			ℓ_2 radius r (%)		
		0.0	0.50	1.0	0.0	0.50	1.0	0.0	0.50	1.0
RS	0.25	92.8	45.7	0	94.6	53.2	10.5	77.4	43.5	15.7
	0.50	87.7	47.8	10.5	89.3	52.1	12.2	73.3	39.9	21.8
	1.0	81.4	51.6	18.8	84.7	54.3	21.2	66.4	42.9	22.8
ARS	0.25	95.2	53.3	27.4	96.7	57.4	31.3	79.1	58.4	32.5
	0.50	91.3	53.9	30.4	91.9	55.1	32.8	74.9	54.7	33.3
	1.0	85.3	59.2	31.6	86.9	57.4	34.6	69.9	52.9	34.1
HyCAS	0.25	96.8	58.1	33.7	97.2	60.5	35.4	81.6	61.9	38.6
	0.50	92.7	59.3	34.8	93.1	60.4	36.6	76.2	58.6	40.9
	1.0	87.7	62.3	36.9	88.2	61.9	38.5	71.7	60.6	41.4

3. **Randomised Attention Noise Injection (RANI)**. Given the 1-Lipschitz projection output $h = \text{Conv}(Ux; W_{\text{SN}})$, draw internal randomness ω and apply a *data-independent* bounded mask $M_\omega \in [0, 1]^d$ through the RANI module $R(h; M_\omega)$. For newly drawn ω , $\|I + D_{M_\omega}\|_2 \leq \|I\|_2 + \|D_{M_\omega}\|_2 \leq 2$; therefore the composite map $x \mapsto R(\text{Conv}(Ux; W_{\text{SN}}); \omega)$ is 2-Lipschitz. This couples the spectrally normalised random projection with RANI, injecting refined stochasticity while multiplying the stream’s Lipschitz constant by at most 2 (ref. Proposition 2; see also App. A.2 for the residual bound). Define the 1-Lip core $H_{\text{RPFAN}}(x) = \text{Conv}(Ux; W_{\text{SN}})$ and the stream output as:

$$G_{\text{RPFAN}}(x; \psi, M_\omega) = H_{\text{RPFAN}}(x; \psi) + R(H_{\text{RPFAN}}(x; \psi); M_\omega); \quad (7)$$

then $\text{Lip}(G_{\text{RPFAN}}) \leq 2$ (See Proof 5).

Therefore, RPFAN minimises the objective of HyCAS by incorporating refined stochasticity into the network through RPF and RANI modules:

$$\mathcal{L}_{\text{RPFAN}}(\theta) = \min_{\theta} \mathbb{E}_{(x,y)} \mathbb{E}_{\varepsilon \sim \mathcal{N}(0, \sigma^2 I), \Omega} \ell(f_\theta(x + \varepsilon; \Omega), y). \quad (8)$$

3.4 RANI: RANDOMIZED ATTENTION NOISE INJECTION

Motivation. Certified deterministic 1-Lipschitz defenses (e.g., SNC) bound the worst–case ℓ_2 perturbation but still expose a deterministic gradient field that adversaries can exploit. Classical randomized defenses inject noise only at the input, whereas certified Lipschitz defenses remain deterministic inside the network. **RANI** closes this gap: it injects a *data-independent*, stochastic *attention mask* $M_\omega \in [0, 1]^d$ after every spectrally-normalised block in the three streams (FDPAN, RPFAN, SNCAN) and once more at their fused output, while preserving a global 2-Lipschitz envelope. Formally, the deterministic 1-Lipschitz map $h \in H(x; \xi, \psi)$ is replaced by the stochastic 2-Lipschitz map $\hat{h} \in R(h; M_\omega)$ via incorporating RANI module ($R(\cdot; M_\omega)$).

Attention noise mechanism. For each forward pass, RANI draws fresh noise $\omega \sim \mathcal{N}(0, I)$ for internal randomness and computes a bounded attention noise $M_\omega \in [0, 1]^d$ that is *independent of the current features*. For any deterministic feature tensor $h \in \mathbb{R}^{H \times W \times C}$, we modulate it according to:

$$\hat{h} = h \odot M_\omega, \quad (9)$$

where \odot denotes the Hadamard product. This yields a Lipschitz constant of at most 2; hence every block’s constant grows from 1 – *Lipschitz* deterministic to a *randomised defense* (see Appendix A.3 (Lemma 3)).

In practice, M_ω is produced by our RANI module via injecting noise at local and channel information of the given deterministic feature maps (e.g., $h \in H(x; \xi, \psi)$); (See Appendix A.6 for more details of our RANI module. The following lemma states the guarantee formally.

Lemma 1 (RANI module is 2-Lipschitz). *Let $h \in \mathbb{R}^d$ and let $M(\omega) \in [0, 1]^d$ be sampled i.i.d. from an arbitrary distribution that is independent of h . Define the RANI mapping as shown in Eq. 9. Then, for each randomly drawn ω and any h_1, h_2 , the mapping \hat{h} is 2-Lipschitz with respect to the Euclidean norm $\|\cdot\|_2$; i.e.,*

$$\|R(h_1; M_\omega) - R(h_2; M_\omega)\|_2 \leq 2 \|h_1 - h_2\|_2.$$

Proof. See proof within the Appendix A.3. □

Table 3: Robust accuracy (%) against ℓ_∞ attacks (APGD-20 and AA-20) on NIH-CXR (left) and NCT-CRC-HE-100K (right) at $\epsilon \in \{8/255, 16/255\}$.

Method	NIH-CXR					NCT-CRC-HE-100K				
	Clean	APGD-20		AA-20		Clean	APGD-20		AA-20	
		8/255	16/255	8/255	16/255		8/255	16/255	8/255	16/255
AT	89.1 ± 1.91	74.7 ± 2.52	66.9 ± 3.41	74.2 ± 2.93	64.1 ± 3.70	92.2 ± 1.82	77.8 ± 2.51	68.7 ± 3.12	76.3 ± 2.83	66.2 ± 3.61
RPF	88.4 ± 1.82	83.7 ± 2.49	71.9 ± 3.29	82.5 ± 2.71	70.8 ± 3.52	91.1 ± 1.71	86.1 ± 2.33	73.9 ± 3.33	84.2 ± 2.62	72.4 ± 3.41
CTRW	88.4 ± 1.73	85.1 ± 2.23	73.1 ± 3.22	84.5 ± 2.48	72.6 ± 3.41	90.4 ± 1.62	87.6 ± 2.29	76.7 ± 3.12	86.7 ± 2.44	75.2 ± 3.22
DCS	87.2 ± 2.05	82.4 ± 2.41	71.7 ± 3.21	81.7 ± 2.72	69.6 ± 3.45	90.3 ± 1.93	84.5 ± 2.72	73.0 ± 3.25	83.3 ± 2.74	71.6 ± 3.46
ARS	84.8 ± 2.22	75.1 ± 3.01	64.7 ± 3.28	72.8 ± 3.11	62.8 ± 3.72	86.8 ± 2.14	75.9 ± 2.71	66.1 ± 3.52	74.6 ± 3.11	64.5 ± 3.73
DRS	83.9 ± 2.33	73.1 ± 2.41	62.9 ± 3.23	71.6 ± 3.12	61.9 ± 3.81	85.9 ± 2.25	75.1 ± 2.61	65.2 ± 3.82	73.5 ± 3.21	63.7 ± 3.94
HyCAS	89.5 ± 1.64	88.6 ± 2.33	77.3 ± 3.14	86.9 ± 2.42	74.4 ± 3.33	91.3 ± 2.63	90.4 ± 2.82	79.3 ± 3.52	88.2 ± 2.63	76.7 ± 3.34

Table 4: Robust accuracy (%) against ℓ_∞ attacks (APGD-20 and AA-20) on HAM10000 (left) and EyePACS (right) at $\epsilon \in \{8/255, 16/255\}$.

Method	HAM10000					EyePACS				
	Clean	APGD-20		AA-20		Clean	APGD-20		AA-20	
		8/255	16/255	8/255	16/255		8/255	16/255	8/255	16/255
AT	75.2 ± 2.94	56.1 ± 3.49	46.5 ± 3.75	54.2 ± 3.93	44.2 ± 3.80	78.2 ± 2.91	60.0 ± 2.72	50.1 ± 3.52	58.3 ± 2.83	48.2 ± 3.61
RPF	74.3 ± 2.86	64.1 ± 3.41	51.9 ± 3.42	62.6 ± 3.71	50.4 ± 3.58	77.1 ± 2.90	67.8 ± 2.57	56.1 ± 3.12	66.4 ± 2.73	54.4 ± 3.44
CTRW	74.3 ± 2.75	64.7 ± 3.33	52.8 ± 3.32	63.3 ± 3.48	51.2 ± 3.52	76.4 ± 2.84	70.1 ± 2.53	57.7 ± 3.35	69.7 ± 2.64	56.1 ± 3.31
DCS	73.2 ± 2.94	62.9 ± 3.48	51.7 ± 3.09	61.4 ± 3.72	49.5 ± 3.45	76.4 ± 2.94	66.8 ± 2.53	55.2 ± 3.68	65.3 ± 2.74	53.6 ± 3.46
ARS	69.8 ± 3.22	53.9 ± 3.88	44.1 ± 3.13	52.7 ± 4.10	42.8 ± 3.71	72.9 ± 3.97	59.9 ± 2.91	48.8 ± 3.61	57.6 ± 2.94	46.5 ± 3.73
DRS	68.9 ± 3.28	53.4 ± 3.84	43.2 ± 3.43	51.6 ± 4.12	41.8 ± 3.81	71.9 ± 3.86	58.3 ± 2.61	47.4 ± 3.71	56.5 ± 2.92	45.7 ± 3.94
HyCAS	74.6 ± 2.74	67.8 ± 3.43	55.3 ± 3.14	65.8 ± 3.42	53.1 ± 3.33	77.6 ± 2.79	72.6 ± 2.72	60.5 ± 3.43	71.8 ± 2.82	58.3 ± 3.32

Therefore, RANI minimises the objective of HyCAS by incorporating refined stochasticity into the network:

$$\mathcal{L}_{\text{RANI}}(\theta) = \min_{\theta} \mathbb{E}_{(x,y)} \mathbb{E}_{\epsilon \sim \mathcal{N}(0, \sigma^2 I), M_\omega} \ell(f_\theta(x + \epsilon; M_\omega), y), \quad (10)$$

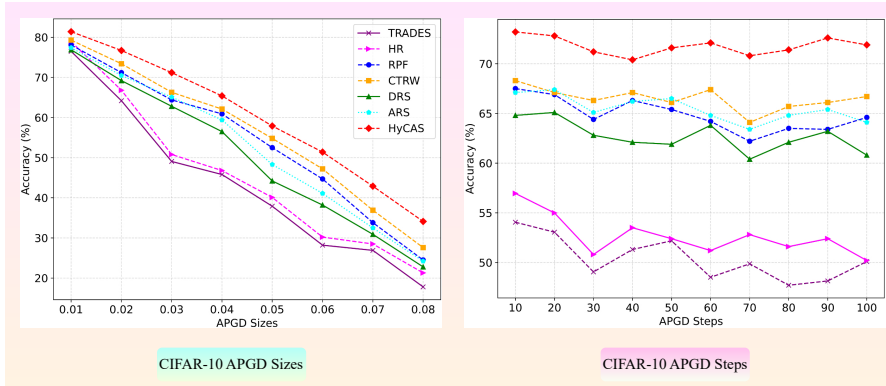


Figure 2: Empirical robustness of HyCAS versus leading baselines (RPF, CTRW, DRS, ARS) on CIFAR-10 under strong APGD attacks. We evaluate two settings: (1) perturbation sizes ϵ from 0.01 to 0.08 and (2) iteration steps from 10 to 100.

4 EXPERIMENT RESULT

4.1 EXPERIMENT SETUP

Evaluation protocol. We evaluate HyCAS on eight vision benchmarks (CIFAR-10/100 (Krizhevsky, 2009), ImageNet-1k (Deng et al., 2009), CelebA (Liu et al., 2015), NCT-CRC-HE-100K (Kather et al., 2018), NIH-CXR (Wang et al., 2017), EyePACS (EyePACS, 2015), and HAM10000 (Tschandl et al., 2018)). We report *certified accuracy* at preset ℓ_2 radii r for smoothing noise levels $\sigma \in \{0.25, 0.50, 1.0, 2.0\}$.

Empirical robustness is measured under ℓ_∞ APGD-20 (Croce & Hein, 2020)² and AutoAttack (AA) (Croce & Hein, 2020) at budgets $\epsilon \in \{8/255, 16/255\}$. We also evaluate HyCAS under

²We use the combination of ℓ_∞ -APGD_{CE} and ℓ_∞ -APGD_{T-DLR} from (Croce & Hein, 2020), each run for 20 iterations with 5 random restarts; we denote this union as APGD-20.

stronger APGD settings with larger ϵ and more attack steps (Figs. 2–4). Baselines span randomized smoothing methods (RS (Cohen et al., 2019), IRS (Ugare et al.), DRS (Xia et al., 2024)), ARS (Lyu et al., 2024), and 1-Lipschitz defenses (LOT (Xu et al., 2022), SLL (Araujo et al., 2023)). *All experiments are run with five random seeds, and we report the mean, the standard deviation, or both for each experiment.* Implementation details, certification and empirical settings are in Appendix A.8.

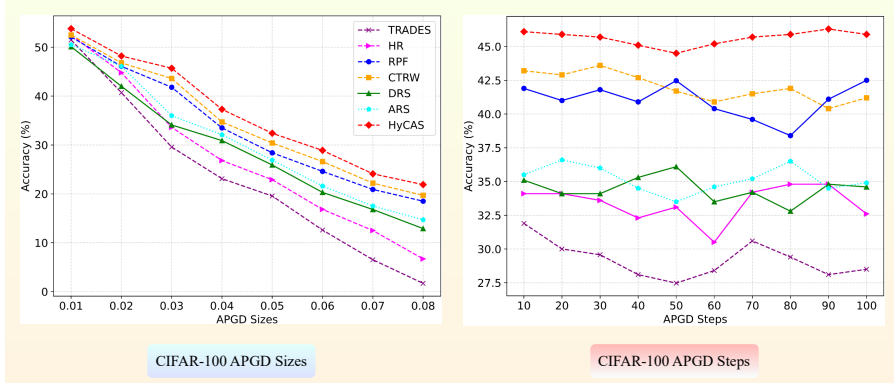


Figure 3: Empirical robustness of HyCAS versus leading baselines (RPF, CTRW, DRS, ARS) on CIFAR-100 under strong APGD attacks. We evaluate two settings: (1) perturbation sizes ϵ from 0.01 to 0.08 and (2) iteration steps from 10 to 100.

4.2 CERTIFIED ADVERSARIAL ROBUSTNESS AT PRESET RADII

CIFAR-10 and ImageNet. Across all baselines in Table 1, HyCAS achieves the best certified accuracy for every (r, σ) pair. On the CIFAR-10, at the representative medium radius $r=0.75$, it yields **44.3%** certified accuracy for both $\sigma \in \{0.25, 0.50\}$ —an gain of 5.2–18.2% over the prior methods. Even in the large-radius tail ($r=2.0, \sigma = 0.50$), it retains **12.5%**, surpassing the leading baseline by 4.0–12.5%. A similar trend emerges on ImageNet: in the large-radius regime ($r = 1.5, \sigma = 0.50$), HyCAS reaches **32.7%** certified accuracy, exceeding every baseline by 2.1–32.7%. HyCAS also delivers state-of-the-art clean accuracy—85.4% on CIFAR-10 and 72.3% on ImageNet—modestly but consistently ahead of all baselines.

Skin, Chest Xray, and Face datasets. Table 2 demonstrates the same dominance beyond CIFAR-10 and ImageNet datasets. On the CelebA dataset, HyCAS achieves certified accuracies of **62.3%** at $r = 0.5$ and **36.9%** at $r = 1.0$, outperforming RS and ARS by 5.3–18.1%. For the HAM10000 dataset, it reaches **61.9%** (at $r = 0.5$) and **38.5%** (at $r = 1.0$), leading all baselines by approximately 4%. On the NIH-CXR dataset, certified accuracy spans **61.9%** (at $r = 0.5, \sigma = 0.25$) to **41.4%** (at $r = 1.0, \sigma = 1.0$), a gain of 3.5–7.3% over the leading baseline (e.g., ARS). Clean accuracy is likewise higher or on par across the board, ranging from 81.6–97.2%.

Effect of the noise level. Increasing the smoothing noise σ consistently trades a negligible drop at small radii for substantial gains at large radii across *every* baseline, yielding a tunable accuracy–robustness frontier. For example, on CIFAR-10, raising σ from 0.25 to 0.50 leaves performance at $r = 0.75$ unchanged (44.3%) yet improves $r = 2.0$ from 8.52% to 12.5%. The same adjustment on ImageNet elevates $r = 2.0$ from 5.42% to 24.8%. These monotonic improvements confirm that HyCAS provides a controllable, rather than fixed, trade-off curve.

4.3 EMPIRICAL ADVERSARIAL ROBUSTNESS

Across our empirical evaluations (Tables 3–4), HyCAS achieves the highest robust top-1 accuracy under APGD-20 and AA-20 at $\epsilon \in \{8, 16\}/255$. Specifically, on the NIH-CXR benchmark, HyCAS retains robust accuracy, outperforming the leading baseline (CTRW) by about **+1.8–4.2%** across these attacks while maintaining similar clean-set accuracy (89.5% vs. 88.4%). A similar trend appears on the NCT-CRC-HE-100K dataset, where HyCAS records robust accuracies of **76.7–79.3%** at $\epsilon = 16/255$ against the same attacks, exceeding CTRW by roughly **+1.5–2.6%** and leaving earlier certified defences (e.g., ARS, DRS) more than **+12%** behind at this stronger perturbation level. Dermoscopic HAM10000 and fundus-image EyePACS exhibit the same hierarchy: HyCAS secures robust accuracies of **53.1–67.8%** against APGD-20 and AA-20 attacks on HAM10000—around **+1.9–3.1%** better than the next-best adversarial defence—and widens the margin on EyePACS to

58.3–72.6%, thereby surpassing the leading baseline CTRW by approximately **+2.1–2.8%**. Together, these results show that HyCAS transfers its randomized Lipschitz strategy from certification to empirical regimes, maintaining clean accuracy while achieving state-of-the-art adversarial robustness.

Under stronger APGD attacks on CIFAR-10/100 (Figs. 2–3), HyCAS outperforms all baselines and preserves its advantage as attack strength increases. On CIFAR-10, when the perturbation radius is varied from $\epsilon = 0.01$ to 0.08, HyCAS traces the upper envelope of the robust-accuracy curves, retaining an $\approx 10\%$ advantage at the largest perturbation, where leading methods collapse. A similar trend holds on CIFAR-100 as the number of APGD iterations increases from **10 to 100**: all prior defenses, including TRADES (Zhang et al., 2019) and HR (Bennouna et al., 2023), degrade monotonically, whereas HyCAS declines more gracefully and remains **7–12%** above the closest competitor at 100 steps, confirming that its internally resampled attention noise and random projections thwart extended optimization. Thus, this randomized, Lipschitz-constrained design scales gracefully with both perturbation size and steps, offering adversarial robustness and a broader safety margin.

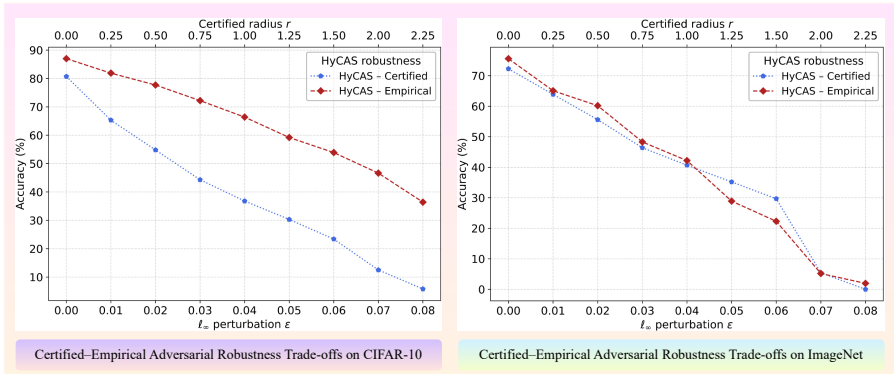


Figure 4: Trade-off between certified and empirical adversarial robustness achieved by HyCAS on the CIFAR-10 (Left) and ImageNet (Right) datasets.

4.4 CERTIFIED-EMPIRICAL ROBUSTNESS TRADE-OFF

Figure 4 plots HyCAS on a three-axis Pareto frontier that couples certified ℓ_2 accuracy (radius r) with empirical ℓ_∞ robustness (APGD-20 accuracy at perturbation strength ϵ). Across both CIFAR-10 and ImageNet, the frontier is smooth and strictly downward-sloping: as the certified radius widens, empirical robustness inevitably contracts. Two consistent phenomena stand out: (a) **Certificate conservativeness**. For the small perturbation regime (left-most region), the empirical curve lies markedly above the certified curve, confirming that formal certificates are—by design—pessimistic relative to observed robustness. (b) **Norm mismatch tail-gap**. At large radii/perturbation strength (right-most region), the gap widens further, highlighting the inherent difficulty of translating ℓ_2 guarantees into ℓ_∞ performance.

HyCAS achieves this trade-off by increasing the smoothing noise from $\sigma = 0.25$ to 0.50 (arrow along each curve) leaves mid-radius performance virtually unchanged, yet extends both certified and empirical robustness deep into the high-perturbation regime. On CIFAR-10, certified accuracy at radius $r = 2.0$ improves from 8.5% to 12.5%, while ImageNet shows an even larger jump—from 5.4% to 24.8%—at the same radius. Crucially, these gains incur **minimal loss** in clean-accuracy / small- ϵ robustness, giving this *state-of-the-art adversarial defense* a **knob** to dial the desired security level without wholesale accuracy sacrifice. See Appendix A.9 for additional experiments and Appendices A.10-A.11 for detailed ablations and certified and empirical robustness discussions.

5 CONCLUSION

We presented HyCAS, a randomized adversarial defence whose deterministic 1-Lipschitz architecture is incorporated with two forms of data-independent internal randomness, yielding a global ≤ 2 -Lipschitz network and a simple margin-based ℓ_2 certificate. Experiments on diverse imaging benchmarks demonstrate state-of-the-art certified accuracy and strong empirical robustness against powerful ℓ_∞ attacks. Future work includes deriving tighter ℓ_∞ certificates, designing lighter-weight certification samplers, and integrating HyCAS into multi-modal clinical pipelines.

REFERENCES

- Motasesm Alfarra, Adel Bibi, Philip HS Torr, and Bernard Ghanem. Data dependent randomized smoothing. In *Uncertainty in Artificial Intelligence*, pp. 64–74. PMLR, 2022a.
- Motasesm Alfarra, Juan C Pérez, Ali Thabet, Adel Bibi, Philip HS Torr, and Bernard Ghanem. Combating adversaries with anti-adversaries. In *Proceedings of the AAAI Conference on Artificial Intelligence*, volume 36, pp. 5992–6000, 2022b.
- Alexandre Araujo, Aaron Havens, Blaise Delattre, Alexandre Allauzen, and Bin Hu. A unified algebraic perspective on lipschitz neural networks. *arXiv preprint arXiv:2303.03169*, 2023.
- Anish Athalye, Nicholas Carlini, and David Wagner. Obfuscated gradients give a false sense of security: Circumventing defenses to adversarial examples. In *International Conference on Machine Learning (ICML)*, 2018.
- Amine Bennouna, Ryan Lucas, and Bart Van Parys. Certified robust neural networks: Generalization and corruption resistance. In *International Conference on Machine Learning*, pp. 2092–2112. PMLR, 2023.
- Yulong Cao, Ningfei Wang, Chaowei Xiao, Dawei Yang, Jin Fang, Ruigang Yang, Qi Alfred Chen, Mingyan Liu, and Bo Li. Invisible for both camera and lidar: Security of multi-sensor fusion based perception in autonomous driving under physical-world attacks. In *2021 IEEE Symposium on Security and Privacy (SP)*, 2021.
- Nicholas Carlini and David A. Wagner. Towards evaluating the robustness of neural networks. In *IEEE Symposium on Security and Privacy (SP)*, pp. 39–57, 2017. doi: 10.1109/SP.2017.49.
- Nicholas Carlini, Florian Tramèr, Krishnamurthy Dvijotham, Leslie Rice, Mingjie Sun, and J. Zico Kolter. (certified!!) adversarial robustness for free! In *International Conference on Learning Representations (ICLR)*, 2023.
- Zhiyuan Cheng, James Chenhao Liang, Guanhong Tao, Dongfang Liu, and Xiangyu Zhang. Adversarial training of self-supervised monocular depth estimation against physical-world attacks. In *International Conference on Learning Representations (ICLR)*, 2023.
- Jeremy Cohen, Elan Rosenfeld, and Zico Kolter. Certified adversarial robustness via randomized smoothing. In *International Conference on Machine Learning (ICML)*, 2019.
- Francesco Croce and Matthias Hein. Reliable evaluation of adversarial robustness with an ensemble of diverse parameter-free attacks. In *International conference on machine learning*, pp. 2206–2216. PMLR, 2020.
- Francesco Croce, Sven Gowal, Thomas Brunner, Evan Shelhamer, Matthias Hein, and Taylan Cemgil. Evaluating the adversarial robustness of adaptive test-time defenses. In *International Conference on Machine Learning (ICML)*, pp. 4421–4435, 2022.
- Jia Deng, Wei Dong, Richard Socher, Li-Jia Li, Kai Li, and Li Fei-Fei. ImageNet: A large-scale hierarchical image database. In *IEEE Conference on Computer Vision and Pattern Recognition (CVPR)*, 2009.
- Joy Dhar, Puneet Goyal, Maryam Haghighat, Nayyar Zaidi, Ferdous Sohel, Bao Q Vo, and KC Santosh. Towards building robust models for unimodal and multimodal medical imaging data. *Information fusion*, pp. 103822, 2025.
- Joy Dhar, Nayyar Zaidi, and Maryam Haghighat. Effective and robust multimodal medical image analysis. *arXiv preprint arXiv:2602.15346*, 2026.
- Gavin Weiguang Ding, Luyu Wang, Xiaomeng Jin, Furui Liu, Yash Sharma, Adam Yala, and Ruitong Huang. MMA training: Direct input space margin maximization through adversarial training. In *International Conference on Learning Representations (ICLR)*, 2019.
- Minjing Dong and Chang Xu. Adversarial robustness via random projection filters. In *Proceedings of the IEEE/CVF Conference on Computer Vision and Pattern Recognition*, pp. 4077–4086, 2023.

- Ranjie Duan, Yuefeng Chen, Dantong Niu, Yun Yang, A. Kai Qin, and Yuan He. AdvDrop: Adversarial attack to DNNs by dropping information. In *IEEE/CVF International Conference on Computer Vision (ICCV)*, 2021.
- EyePACS. EyePACS diabetic retinopathy detection dataset. <https://www.kaggle.com/c/diabetic-retinopathy-detection>, 2015. Accessed 18 Sep 2025.
- Henry Gouk, Eibe Frank, Bernhard Pfahringer, and Michael J. Cree. Regularisation of neural networks by enforcing lipschitz continuity. *Machine Learning*, 110(2):393–416, 2021. doi: 10.1007/s10994-020-05908-7.
- Zhongkai Hao, Chengyang Ying, Yinpeng Dong, Hang Su, Jian Song, and Jun Zhu. GSmooth: Certified robustness against semantic transformations via generalized randomized smoothing. In *International Conference on Machine Learning (ICML)*, 2022.
- Kaiming He, Xiangyu Zhang, Shaoqing Ren, and Jian Sun. Deep residual learning for image recognition. In *IEEE Conference on Computer Vision and Pattern Recognition (CVPR)*, 2016.
- Zhezhi He, Adnan Siraj Rakin, and Deliang Fan. Parametric noise injection: Trainable randomness to improve deep neural network robustness against adversarial attack. In *Proceedings of the IEEE/CVF conference on computer vision and pattern recognition*, pp. 588–597, 2019.
- Dan Hendrycks, Kevin Zhao, Steven Basart, Jacob Steinhardt, and Dawn Song. Natural adversarial examples. In *Proceedings of the IEEE/CVF conference on computer vision and pattern recognition*, pp. 15262–15271, 2021.
- Hanbin Hong, Binghui Wang, and Yuan Hong. UniCR: Universally approximated certified robustness via randomized smoothing. In *European Conference on Computer Vision (ECCV)*, 2022.
- Roger A Horn and Charles R Johnson. *Matrix analysis*. Cambridge university press, 2012.
- Ahmadreza Jeddi, Mohammad Javad Shafiee, Michelle Karg, Christian Scharfenberger, and Alexander Wong. Learn2perturb: An end-to-end feature perturbation learning to improve adversarial robustness. In *IEEE/CVF Conference on Computer Vision and Pattern Recognition (CVPR)*, pp. 1241–1250, 2020.
- Jongheon Jeong and Jinwoo Shin. Consistency regularization for certified robustness of smoothed classifiers. In *Advances in Neural Information Processing Systems (NeurIPS)*, 2020.
- Jakob Nikolas Kather, Niels Halama, and Alexander Marx. 100,000 histological images of human colorectal cancer and healthy tissue, 2018. URL <https://doi.org/10.5281/zenodo.1214456>. Dataset: NCT-CRC-HE-100K.
- Alex Krizhevsky. Learning multiple layers of features from tiny images. Technical report, University of Toronto, 2009.
- Mathias Lécuyer, Vaggelis Atlidakis, Roxana Geambasu, Daniel Hsu, and Suman Jana. Certified robustness to adversarial examples with differential privacy. In *IEEE Symposium on Security and Privacy (SP)*, pp. 656–672, 2019. doi: 10.1109/SP.2019.00066.
- Qizhang Li, Yiwen Guo, Wangmeng Zuo, and Hao Chen. Making substitute models more bayesian can enhance transferability of adversarial examples. *arXiv preprint arXiv:2302.05086*, 2023.
- Hongbin Liu, Jinyuan Jia, and Neil Zhenqiang Gong. Pointguard: Provably robust 3d point cloud classification. In *Proceedings of the IEEE/CVF conference on computer vision and pattern recognition*, pp. 6186–6195, 2021.
- Ziwei Liu, Ping Luo, Xiaogang Wang, and Xiaoou Tang. Deep learning face attributes in the wild. In *Proceedings of the IEEE International Conference on Computer Vision (ICCV)*, 2015.
- Saiyue Lyu, Shadab Shaikh, Frederick Shpilevskiy, Evan Shelhamer, and Mathias Lécuyer. Adaptive randomized smoothing: Certified adversarial robustness for multi-step defences. *Advances in Neural Information Processing Systems*, 37:134043–134074, 2024.

- Yanxiang Ma, Minjing Dong, and Chang Xu. Adversarial robustness through random weight sampling. In *Advances in Neural Information Processing Systems (NeurIPS)*, 2023.
- Aleksander Madry, Aleksandar Makelov, Ludwig Schmidt, Dimitris Tsipras, and Adrian Vladu. Towards deep learning models resistant to adversarial attacks. In *International Conference on Learning Representations (ICLR)*, 2018.
- Takeru Miyato, Toshiki Kataoka, Masanori Koyama, and Yuichi Yoshida. Spectral normalization for generative adversarial networks. In *International Conference on Learning Representations (ICLR)*, 2018.
- Apapan Pumsirirat and Yan Liu. Credit card fraud detection using deep learning based on auto-encoder and restricted boltzmann machine. *International Journal of Advanced Computer Science and Applications (IJACSA)*, 2018.
- Aditi Raghunathan, Jacob Steinhardt, and Percy Liang. Certified defenses against adversarial examples. In *International Conference on Learning Representations (ICLR)*, 2018.
- Leslie Rice, Eric Wong, and J. Zico Kolter. Overfitting in adversarially robust deep learning. In *Proceedings of the International Conference on Machine Learning*, pp. 8093–8104. PMLR, November 2020.
- Hadi Salman, Jerry Li, Ilya Razenshteyn, Pengchuan Zhang, Huan Zhang, Sébastien Bubeck, and Greg Yang. Provably robust deep learning via adversarially trained smoothed classifiers. In *Advances in Neural Information Processing Systems (NeurIPS)*, 2019.
- Hanie Sedghi, Vineet Gupta, and Philip M Long. The singular values of convolutional layers. *arXiv preprint arXiv:1805.10408*, 2018.
- Ali Shafahi, Mahyar Najibi, Mohammad Amin Ghiasi, Zheng Xu, John Dickerson, Christoph Studer, Larry S. Davis, Gavin Taylor, and Tom Goldstein. Adversarial training for free! In *Advances in Neural Information Processing Systems (NeurIPS)*, 2019.
- Gaurang Sriramanan, Sravanti Addepalli, Arya Baburaj, et al. Towards efficient and effective adversarial training. In *Advances in Neural Information Processing Systems (NeurIPS)*, 2021.
- Peter Šúkeník, Aleksei Kuvshinov, and Stephan Günnemann. Intriguing properties of input-dependent randomized smoothing. In *International Conference on Machine Learning (ICML)*, 2022.
- Florian Tramèr, Nicholas Carlini, Wieland Brendel, and Aleksander Madry. On adaptive attacks to adversarial example defenses. In *Advances in Neural Information Processing Systems (NeurIPS)*, pp. 1633–1645, 2020.
- Philipp Tschandl, Cliff Rosendahl, and Harald Kittler. The HAM10000 dataset: A large collection of multi-source dermatoscopic images of common pigmented skin lesions. *Scientific Data*, 5: 180161, 2018. doi: 10.1038/sdata.2018.161.
- Shubham Ugare, Tarun Suresh, Debangshu Banerjee, Gagandeep Singh, and Sasa Misailovic. Incremental randomized smoothing certification. In *The Twelfth International Conference on Learning Representations*.
- Xiaosong Wang, Yifan Peng, Le Lu, Zhiyong Lu, Mohammadhadi Bagheri, and Ronald M. Summers. ChestX-ray8: Hospital-scale chest x-ray database and benchmarks on weakly-supervised classification and localization of common thorax diseases. In *Proceedings of the IEEE Conference on Computer Vision and Pattern Recognition (CVPR)*, pp. 3462–3471, 2017. doi: 10.1109/CVPR.2017.369. Dataset: NIH ChestX-ray (ChestX-ray8/14).
- Eric Wong and J. Zico Kolter. Provable defenses against adversarial examples via the convex outer adversarial polytope. In *International Conference on Machine Learning (ICML)*, 2018.
- Song Xia, Yi Yu, Xudong Jiang, and Henghui Ding. Mitigating the curse of dimensionality for certified robustness via dual randomized smoothing. In *ICLR*, 2024.

- Kun Xiang, Xing Zhang, Jinwen She, Jinpeng Liu, Haohan Wang, Shiqi Deng, and Shancheng Jiang. Toward robust diagnosis: A contour attention preserving adversarial defense for covid-19 detection. In *AAAI Conference on Artificial Intelligence (AAAI)*, volume 37, pp. 2928–2937, 2023.
- Xiaojun Xu, Linyi Li, and Bo Li. Lot: Layer-wise orthogonal training on improving l2 certified robustness. *Advances in Neural Information Processing Systems*, 35:18904–18915, 2022.
- Zhuolin Yang, Linyi Li, Xiaojun Xu, Bhavya Kailkhura, Tao Xie, and Bo Li. On the certified robustness for ensemble models and beyond. In *International Conference on Learning Representations*, 2022.
- Zheng Yuan, Jie Zhang, Yunpei Jia, Chuanqi Tan, Tao Xue, and Shiguang Shan. Meta gradient adversarial attack. In *IEEE/CVF International Conference on Computer Vision (ICCV)*, 2021.
- Hongyang Zhang, Yaodong Yu, Jiantao Jiao, Eric Xing, Laurent El Ghaoui, and Michael Jordan. Theoretically principled trade-off between robustness and accuracy. In *International conference on machine learning*, pp. 7472–7482. PMLR, 2019.

A APPENDIX

A.1 ADDITIONAL RELATED STUDY

Note that: in the Table 5, we compare the properties for novel adversarial defense approach for enhancing adversarial robustness against existing baselines, demonstrating how *HyCAS* uniquely overcomes each identified research gap.

A.2 PRELIMINARIES

A.2.1 RANDOMIZED SMOOTHING (RS)

Consider a k -class classification problem with input $x \in \mathbb{R}^d$ and label $y \in \mathcal{Y} = \{c_1, \dots, c_k\}$. RS first corrupts each input x by adding isotropic Gaussian noise $\mathcal{N}(\varepsilon; 0, \sigma^2 I)$. It then turns an arbitrary base classifier f into a smoothed version F that possesses ℓ_2 certified robustness guarantees. The smoothed classifier F returns whichever class the base classifier f is most likely to return under the distribution $\mathcal{N}(x + \varepsilon; x, \sigma^2 I)$,

$$F(x) = \arg \max_{c \in \mathcal{Y}} \Pr(f(x + \varepsilon) = c). \quad (11)$$

Theorem 2 (Cohen et al., 2019). *Let $f: \mathbb{R}^d \rightarrow \mathcal{Y}$ be any deterministic or random function, and let F be the smoothed version defined in Equation equation 11. Let c_A and c_B be the most probable and runner-up classes returned by F with smoothed probabilities p_A and p_B , respectively. Then $F(x + \delta) = c_A$ for all adversarial perturbations δ satisfying*

$$\|\delta\|_2 \leq R', \quad R' = \frac{1}{2} \sigma (\Phi^{-1}(p_A) - \Phi^{-1}(p_B)),$$

where Φ^{-1} is the inverse standard-Gaussian CDF.

In Equation 2, Φ denotes the Gaussian cumulative distribution function (CDF) and Φ^{-1} signifies its inverse function. Theorem 1 indicates that the ℓ_2 certified robustness provided by RS is closely linked to the base classifier’s performance on the Gaussian distribution; a more consistent prediction within a given Gaussian distribution will return a stronger certified robustness. (The proof of Theorem 1 can be found in Appendix A.1.) It is not clear how to calculate p_A and p_B exactly when f is a deep neural network, so Monte Carlo sampling is used to estimate the smoothed probability. The theorem also establishes that, when we assign p_A a lower-bound estimate \underline{p}_A and assign p_B an upper-bound estimate with $\underline{p}_B = 1 - \underline{p}_A$, the radius R' equals

$$R' = \sigma \Phi^{-1}(\underline{p}_A).$$

Equation (3) follows from $-\Phi^{-1}(1 - \underline{p}_A) = \Phi^{-1}(\underline{p}_A)$. The smoothed classifier F is therefore guaranteed to return the constant prediction c_A around x within the ℓ_2 ball of radius R' .

A.2.2 SPECTRAL NORMALISATION OF CONVOLUTIONS

For a kernel $K \in \mathbb{R}^{k_h \times k_w \times C_{in} \times C_{out}}$ we denote by \mathcal{C}_K the induced circular convolution. We follow the two most widely-used operator-norm estimators:

(a) **Exact Fourier bound** (Sedghi et al., 2018) derived

$$\sigma_*(K) = \max_{\omega \in \Omega} \|\widehat{K}(\omega)\|_2, \quad \|\mathcal{C}_K\|_{\text{op}} = \sigma_*(K), \quad (12)$$

which we adopt verbatim in Eq. 12 to scale kernels whenever an FFT is affordable.

(b) **Power-iteration (PI) surrogate** (Miyato et al., 2018) proposed a light T -step estimate, also used by subsequent Lipschitz CNNs. Our implementation in Eq. 13 mirrors their update:

$$\hat{\sigma}^{(T)}(K) = \langle u^{(T)}, \mathcal{C}_K(v^{(T)}) \rangle, \quad (13)$$

with $T=5$ as in their default setting.

Kernel rescaling. Both estimators feed the same renormalisation rule

$$\tilde{K} = \frac{K}{\max\{\hat{\sigma}(K), 1\} + \varepsilon}, \quad \varepsilon = 10^{-6}, \quad (14)$$

which keeps $\|\mathcal{C}_{\tilde{K}}\|_{\text{op}} \leq 1$. (The clamp $\max\{\hat{\sigma}, 1\}$ is a minor safety tweak; we note it here for completeness but do not claim novelty.)

Proposition 3 (Layer-wise 1-Lipschitzness). *Eqs. 12–14 ensure $\|\mathcal{C}_{\tilde{K}}\|_{\text{op}} \leq 1$.*

All subsequent sections treat Eq. 14 as a *black-box deterministic contraction*. Our contribution begins only after this step, in the following Method section.

Proof. Fix ω and let x, y be arbitrary inputs. Define

$$z_x = \mathcal{C}_{\tilde{K}}(x), \quad z_y = \mathcal{C}_{\tilde{K}}(y).$$

Step 1: 1-Lipschitz contraction. By construction of \tilde{K} (Eq. 14) we have

$$\|z_x - z_y\|_2 = \|\mathcal{C}_{\tilde{K}}(x) - \mathcal{C}_{\tilde{K}}(y)\|_2 \leq \|x - y\|_2. \quad (15)$$

Step 2: Bounded multiplicative mask. The mask generated by RANI is *data-independent* for fixed ω , and satisfies the element-wise bound $M(\omega) \in [0, 1]^{H \times W \times C}$. Consequently

$$1 \leq 1 + M(\omega) \leq 2 \quad (\text{element-wise}).$$

For any tensor a this implies

$$\|(1 + M(\omega)) \odot a\|_2 \leq 2\|a\|_2. \quad (16)$$

Step 3: Lipschitz constant of $F(\cdot, \omega)$. Using definition equation 6,

$$F(x, \omega) - F(y, \omega) = (1 + M(\omega)) \odot (z_x - z_y),$$

and therefore, by equation 16 and equation 15,

$$\|F(x, \omega) - F(y, \omega)\|_2 \leq 2\|z_x - z_y\|_2 \leq 2\|x - y\|_2.$$

Because the bound holds for every choice of x, y , the mapping $F(\cdot, \omega)$ is 2-Lipschitz. \square

A.2.3 RANDOM-PROJECTION FILTERS

Random-projection filters (RPF) replace a subset of convolution kernels with i.i.d. Gaussian weights. Let $x \in \mathbb{R}^{H \times W \times C_{\text{in}}}$ be an input, $F \in \mathbb{R}^{k^2 C_{\text{in}} \times C_{\text{out}}}$ the flattened kernel matrix and $z = F^\top x$ the projected feature. When the number of random columns $C_{\text{out}} = N_r$ satisfies the Johnson–Lindenstrauss lower bound,

$$(1 - \varepsilon) \|x_i - x_j\|_2^2 \leq \|z_i - z_j\|_2^2 \leq (1 + \varepsilon) \|x_i - x_j\|_2^2, \quad (17)$$

local geometry is provably preserved (Dong & Xu, 2023). A standard way to keep the mapping 1-Lipschitz is to rescale the frozen kernel with a spectral-norm estimate obtained by a few power-iteration (PI) steps after each forward pass.

A.3 PROOFS

Proof of Theorem 1. By Propositions 2 and 5, SNCAN and RPFAN are ≤ 2 -Lipschitz. By Proposition 1, FDPAN’s gated output is also ≤ 2 -Lipschitz. Finally, Proposition 4 shows the per-channel convex fusion has $\text{Lip}(z) \leq \max_{b \in B} \text{Lip}(G_b) \leq 2$. \square

Proposition 4 (Convex fusion retains the max-Lipschitz). *Given channel-wise convex fusion $z(\cdot)$ (see Eq. 2) that satisfies $\text{Lipschitz}z(z) \leq \max_b \text{Lipschitz}(G_b) \leq 2$, if every stream output is ≤ 2 -Lipschitz, then the Hycas block is also ≤ 2 -Lipschitz.*

Proof of Proposition 4. Fix a channel c and any x, y . Triangle inequality gives

$$\|z(x)_{:,c} - z(y)_{:,c}\| = \left\| \sum_b \alpha_{b,c} (G_b(x)_{:,c} - G_b(y)_{:,c}) \right\| \leq \sum_b \alpha_{b,c} \|G_b(x) - G_b(y)\|.$$

Since $\|G_b(x) - G_b(y)\| \leq L_b \|x - y\|$ and $\sum_b \alpha_{b,c} = 1$, we have $\|z(x)_{:,c} - z(y)_{:,c}\| \leq (\max_b L_b) \|x - y\|$. Taking the maximum over channels yields $\text{Lip}(z) \leq \max_b L_b$. Thus $\text{Lip}(z) \leq 2$. \square

Lemma 2 (Expectation preserves Lipschitz constant). *If $x \mapsto s(x, \Omega)$ is L -Lipschitz for all Ω , then the expected logits $Z(x) = \mathbb{E}_\omega[s(x, \omega)]$ are L -Lipschitz. (By Jensen’s inequality and linearity of expectation (Dong & Xu, 2023).) Hence, HyCAS’s expected classifier inherits the same constant.*

Proof of Lemma 2. For any x, y ,

$$\|Z(x) - Z(y)\| = \|\mathbb{E}_\omega[s(x, \omega) - s(y, \omega)]\| \leq \mathbb{E}_\omega \|s(x, \omega) - s(y, \omega)\| \leq \mathbb{E}_\omega [L \|x - y\|] = L \|x - y\|,$$

using Jensen’s inequality $\|\mathbb{E}X\| \leq \mathbb{E}\|X\|$. \square

Proof of Corollary 1. By Lemma 2, Z is 2-Lipschitz. Hence for any coordinate c ,

$$|Z_c(x + \delta) - Z_c(x)| \leq \|Z(x + \delta) - Z(x)\|_\infty \leq \|Z(x + \delta) - Z(x)\|_2 \leq 2\|\delta\|_2 < \frac{\Delta(x)}{2}.$$

Thus the top logit can decrease by at most $\Delta/2$ and the runner-up can increase by at most $\Delta/2$; their order cannot swap. \square

Proof of Proposition 1. By the triangle inequality and the chain rule for Lipschitz maps,

$$\begin{aligned} \|G_{\text{FDPAN}}(x; \omega) - G_{\text{FDPAN}}(y; \omega)\| &= \|H(x) - H(y) + R(H(x); \omega) - R(H(y); \omega)\| \\ &\leq \|H(x) - H(y)\| + \|R(H(x); \omega) - R(H(y); \omega)\| \\ &\leq \text{Lip}(H) \|x - y\| + \text{Lip}(R) \|H(x) - H(y)\| \\ &\leq 1 \cdot \|x - y\| + 1 \cdot 1 \cdot \|x - y\| = 2 \|x - y\|. \end{aligned}$$

Thus $\text{Lip}(G_{\text{FDPAN}}) \leq 2$. \square

Proof of Proposition 2. Let $x, y \in \mathbb{R}^{H \times W \times C}$ and set $z_1 = C_{K_e}(x)$ and $z_2 = C_{K_e}(y)$. Using equation 5 and the sub-multiplicativity of operator norms,

$$\begin{aligned} \|G_{\text{SNCAN}}(x; M_\omega) - G_{\text{SNCAN}}(y; M_\omega)\|_2 &= \|(I + D_\omega)(z_1 - z_2)\|_2 \\ &\leq \|I + D_\omega\|_2 \|z_1 - z_2\|_2 \\ &\leq 2 \|C_{K_e}(x) - C_{K_e}(y)\|_2 \\ &\leq 2 \|x - y\|_2, \end{aligned}$$

which establishes the claim. \square

Proposition 5 (RPFAN is 2-Lipschitz). *Let U be an orthogonal 1×1 channel mixer ($\|U\|_{\text{op}} = 1$). Let W_{SN} be a spectrally normalized random-projection filter so that the linear map $H_{\text{RPFAN}}(x) := \text{Conv}(Ux; W_{\text{SN}})$ satisfies $\text{Lip}(H_{\text{RPFAN}}) \leq 1$. Let $D_\omega = \text{diag}(M_\omega)$ with $M_\omega \in [0, 1]^d$ and define*

$$G_{\text{RPFAN}}(x; M_\omega) = H_{\text{RPFAN}}(x) + D_\omega H_{\text{RPFAN}}(x) = (I + D_\omega) H_{\text{RPFAN}}(x).$$

Then $\text{Lip}(G_{\text{RPFAN}}) \leq 2$.

Proof of Proposition 5. $\|G(x) - G(y)\| = \|(I + D_\omega)(H_{\text{RPFAN}}(x) - H_{\text{RPFAN}}(y))\| \leq \|I + D_\omega\|_2 \text{Lip}(H_{\text{RPFAN}}) \|x - y\| \leq 2 \cdot 1 \cdot \|x - y\|$. \square

Proof of Lemma 1. Fix any realisation of the noise ω and set $D_\omega = \text{diag}(M_\omega) \in \mathbb{R}^{d \times d}$. By Eq. equation 9 the RANI transformation satisfies

$$R(h; M_\omega) = h + D_\omega h = (I + D_\omega) h.$$

Step 1: bound the operator norm of $I + D_\omega$. Because every coordinate of M_ω lies in $[0, 1]$, each diagonal entry of D_ω is in the same interval. Hence all singular values of D_ω are ≤ 1 and

$$\|I + D_\omega\|_2 \leq \|I\|_2 + \|D_\omega\|_2 = 1 + 1 = 2.$$

Step 2: translate the norm bound into a Lipschitz constant. For arbitrary $h_1, h_2 \in \mathbb{R}^d$,

$$\begin{aligned} \|R(h_1; M_\omega) - R(h_2; M_\omega)\|_2 &= \|(I + D_\omega)(h_1 - h_2)\|_2 \\ &\leq \|I + D_\omega\|_2 \|h_1 - h_2\|_2 \\ &\leq 2 \|h_1 - h_2\|_2. \end{aligned}$$

Therefore $R(\cdot; M_\omega)$ is 2-Lipschitz with respect to the Euclidean norm for every draw of ω , completing the proof. \square

Lemma 3 (Orthogonal transforms are 1-Lipschitz). *If $U \in \mathbb{R}^{d \times d}$ is orthonormal then $\text{Lip}(U) = 1$. In particular, 2-D DCT/IDCT and any frozen orthogonal 1×1 convolution satisfy $\text{Lip} = 1$.*

For a map $h : \mathbb{R}^d \rightarrow \mathbb{R}^d$ the ℓ_2 -Lipschitz constant is

$$\text{Lip}(h) = \sup_{u \neq v} \frac{\|h(u) - h(v)\|_2}{\|u - v\|_2}.$$

Throughout we use the vectorised ℓ_2 norm over $N \times H \times W \times C$ tensors. We make repeated use of: *Triangle inequality.* $\|a + b\|_2 \leq \|a\|_2 + \|b\|_2$. *Convex combination bound.* If $\sum_i \lambda_i = 1$ and $\lambda_i \geq 0$ then $\|\sum_i \lambda_i a_i\|_2 \leq \sum_i \lambda_i \|a_i\|_2$. *Jensen.* $\|\mathbb{E}[X]\|_2 \leq \mathbb{E}[\|X\|_2]$.

Proof of Lemma 3.

$$\|Ux - Uy\| = \|U(x - y)\| = \|x - y\| \quad \text{for all } x, y.$$

\square

Lemma 4 (Spectral normalisation). *Rescaling a convolutional kernel W by $W / \max(\|W\|_2, 1)$ enforces $\text{Lip}(\text{Conv}_W) \leq 1$ (Gouk et al., 2021).*

Proof of Lemma 4. By construction,

$$\|C_{K_c}\|_{\text{op}} = \frac{\|C_K\|_{\text{op}}}{\max\{\sigma^{(K)}, 1\}} \leq \frac{\max\{\|C_K\|_{\text{op}}, \sigma^{(K)}\}}{\max\{\sigma^{(K)}, 1\}} \leq 1.$$

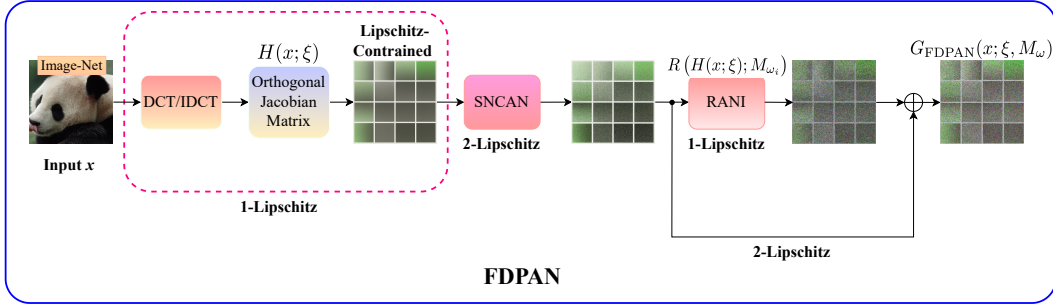
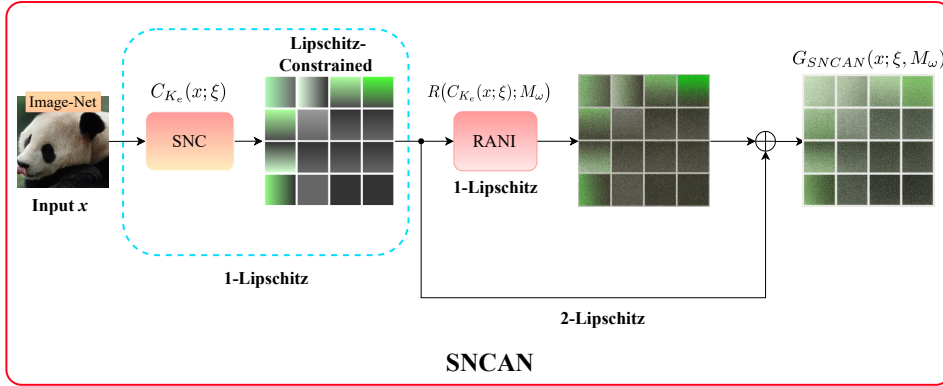
\square

A.4 CERTIFIED PREDICTION UNDER HYPAS

Each HyCAS stream comprises a 1-Lipschitz deterministic core followed by a *data-independent* RANI module. Conditioning on the internal noise ω , each stream is therefore 2-Lipschitz (see Lemma 3), and the composite core remains 2-Lipschitz (ref. Lemma 1). Specifically, the FDPAN stream is the only exception: it contains two residual blocks (SNCAN + RANI), giving a naive 4-Lipschitz upper bound. We tighten this to ≤ 2 -Lipschitz by scaling the skip connection (Proposition 1). A convex channel gate then fuses the streams without increasing the Lipschitz constant (Proposition 4). Finally, stacking modules and applying a global calibrator with gain $c \leq 2/\hat{L}_{\text{net}}$ ensures the entire network is at most 2-Lipschitz.

Table 5: Scope of representative certified, empirical, and hybrid defences. A \checkmark indicates that the property is explicitly addressed, or the domain is reported, in the original paper.

Method	Certified	Empirical	Natural images	Medical images
RS (Cohen et al., 2019)	\checkmark		\checkmark	
IRS (Ugare et al.)	\checkmark		\checkmark	
DRS (Xia et al., 2024)	\checkmark		\checkmark	
ARS (Lyu et al., 2024)	\checkmark		\checkmark	
LOT (Xu et al., 2022)	\checkmark		\checkmark	
SLL (Araujo et al., 2023)	\checkmark		\checkmark	
PNI (He et al., 2019)		\checkmark	\checkmark	
Learn2Perturb (Jeddi et al., 2020)		\checkmark	\checkmark	
CTRW (Ma et al., 2023)		\checkmark	\checkmark	
RPF (Dong & Xu, 2023)		\checkmark	\checkmark	
CAP (Xiang et al., 2023)		\checkmark		\checkmark
HyCAS (ours)	\checkmark	\checkmark	\checkmark	\checkmark

Figure 5: Overview of FDPAN stream. A four-stage cascade: (i) low-pass DCT masking and orthogonal 1×1 channel mix (both 1-Lipschitz); (ii) SNCAN block (spectrally normalized convolution) with RANI; (iii) additional RANI; and (iv) skip/gating. The stream remains ≤ 2 -Lipschitz.Figure 6: Overview of SNCAN block. A spectrally normalized convolution (C_{K_e}) ensures operator norm ≤ 1 ; RANI applies a bounded, data-independent attention mask M_ω so the block output equals $(I + D_\omega) C_{K_e}(x)$, which is ≤ 2 -Lipschitz.

Margin certificate. Define the *expected logits*, averaged only over the model’s internal randomness, be

$$Z(x) = \mathbb{E}_\omega[s(x; \omega)], \text{Lip}(Z) \leq 2 \text{ (Lemma 2).}$$

Let $\Delta_Z(x) = Z_{(1)}(x) - Z_{(2)}(x)$ denote the gap between the top two logits. The certified ℓ_2 radius at x is then,

$$r_2(x) = \frac{\Delta_Z(x)}{4},$$

which guarantees $\arg \max Z(x + \delta) = \arg \max Z(x)$ for every perturbation $\|\delta\|_2 < r_2(x)$ (Corollary 1). For ℓ_∞ , the norm inequality $\|\delta\|_2 \leq \sqrt{d} \|\delta\|_\infty$ yields the conservative certificate $r_\infty(x) = \frac{r_2(x)}{\sqrt{d}}$.

Estimation under internal randomness. At test time we approximate Z through Monte Carlo sampling over ω . Draw n_0 pilot samples to identify the top class, then take n additional samples; compute one-sided confidence bounds for $Z_{(1)}(x)$ and $Z_{(2)}(x)$ and certify with

$$r_{\text{LCB}}(x) = \frac{\text{LCB}(Z_{(1)}(x)) - \text{UCB}(Z_{(2)}(x))}{4},$$

at confidence $1 - \alpha$.

A.5 EXTENDED DETAILS FOR FDPAN, SNCAN, AND RPFAN STREAMS

Detailed overviews of the three parallel streams—FDPAN, SNCAN, and RPFAN—are illustrated in Figs. 5–7, respectively.

A.6 EXTENDED DETAILS FOR RANI MODULE

Deterministic attentions. We design two deterministic attentions—*local* (LA) and *channel* (CA)—that highlight informative local and inter-channel dependencies, respectively. Specifically, we leverage GAP and 1*1 convolution followed by leveraging dense layer and sigmoid to learn these attention maps:

$$LA(z) = \sigma(\text{Conv}_{1 \times 1}^{(l)}(z)), \quad CA(z) = \sigma(\text{Dense}_2^{(l)}(\text{ReLU}(\text{Dense}_1^{(l)}(\text{GAP}(z))))), \quad (18)$$

Injecting stochasticity. We these deterministic attention maps into randomized attention maps (γ'_g and γ'_l) via injecting feature layer noises $\eta_{I_g}, \eta_{I_l} \in \mathbb{R}^C$, thereby incorporating stochasticity. We formulate this as: $\gamma'_g = \eta_{I_g} + g', \quad \gamma'_l = \eta_{I_l} + l',$ (19) where $\sigma_g, \sigma_l \in \mathbb{R}^C$ are trainable scale vectors and $\Psi(u) = \min\{1, \max\{0, u\}\}$ clips the maps into $[0, 1]$.

Noise parameterization and iterative refinement. To realise heteroscedastic, yet data-independent, stochasticity at minimal cost we employ a two-step self-modulation loop

$$\eta_{I_\bullet} = \eta_\bullet \odot (\sigma_\bullet + \eta_\bullet \odot \sigma_\bullet), \quad \bullet \in \{g, l\},$$

This yields two potential benefits: (a) **Richer expressivity**—because σ_\bullet is trainable, the model learns which channels benefit from strong noise and which should stay nearly deterministic; and (b) **Negligible overhead**—only $2C$ extra scalars per branch.

Iterative noise fusion. We propagate the stochastic smoothing through the backbone in *four* stages. At each stage $j \in \{1, \dots, 4\}$ the current feature tensor x'_f is modulated by the noisy randomized the deterministic attention maps, $\Psi(\gamma'_g)_j$ and $\Psi(\gamma'_l)_j$ followed by fuse them as

$$x_U = x'_f \odot \prod_{j=1}^4 [\Psi(\gamma'_g)_j \odot \Psi(\gamma'_l)_j], \quad (20)$$

Each stage injects a freshly resampled attention noise yielding a progressively smoother—stochastic feature tensor. This cascade progressively smooths the feature tensor and presents a continually shifting optimisation landscape to an adversary, thereby enhancing robustness while preserving the global 2-Lipschitz guarantee. Thus RANI converts every deterministic 1-Lipschitz block into a randomised counterpart that keeps the certified ℓ_2 margin while impeding adversarial attacks by presenting a moving optimisation landscape.

A.7 DETAILS ABOUT THE HycAS CERTIFIED ALGORITHM

This section illustrates the details of the certified algorithm of HycAS, as shown in the following subsections:

A.7.1 HycAS TRAINING

Our base network couples a *deterministic, Lipschitz-constrained backbone* with *stochastic smoothing branches*. Concretely, let $f_\theta(\cdot; \Omega)$ denote the hybrid classifier with parameters θ and internal randomness $\Omega = (\psi, M_\omega)$, where ψ parametrizes implicit randomness (e.g., random projection filters) and M_ω injects explicit attention noise. Following randomized smoothing (RS), we expose the input to isotropic Gaussian noise $\varepsilon \sim \mathcal{N}(0, \sigma^2 I)$ during training and minimize the expected loss

$$\min_{\theta} \mathbb{E}_{(x,y)} \mathbb{E}_{\varepsilon \sim \mathcal{N}(0, \sigma^2 I), \Omega} \ell(f_\theta(x + \varepsilon; \Omega), y),$$

which is the same objective used to train the stochastic component in our hybrid architecture (cf. Eq. 10 for RANI in HycAS). To make RS effective at scale while retaining deterministic control, the backbone is constrained to be $L_{\text{net}} \leq 2$ -Lipschitz; our implementation mirrors the HycAS construction where residual blocks are scaled so the stacked network remains ≤ 2 -Lipschitz and thus amenable to margin certification.

To mitigate the curse of dimensionality inherent to RS, we optionally activate a DRS (Dual Randomized Smoothing) path that partitions x into two lower-dimensional sub-inputs and smooths them separately before fusion. This preserves most information while tightening the ℓ_2 certificate upper bound from $O(1/\sqrt{d})$ to $O(1/\sqrt{m} + 1/\sqrt{n})$ with $m + n = d$. Our training simply shares the same θ and minimizes the same expectation, with the forward pass executing the two DRS branches in parallel.

Algorithm 1 summarizes one epoch: for each minibatch we (i) sample (ε, Ω) once per forward; (ii) run the deterministic Lipschitz backbone and the stochastic streams; (iii) backpropagate the Monte-Carlo estimate of the RS objective; and (iv) apply the Lipschitz constraints (spectral normalization / calibrated residual scaling) to keep $L_{\text{net}} \leq 2$.

Algorithm 1 HycAS Training

Requires: Dataset \mathcal{D} ; epochs E ; batch size B ; noise level σ ; HycAS-integrated network f_θ with streams $\{\text{SNCAN}, \text{RPFAN}, \text{FDPAN}\}$, convex channel gate $\alpha_{b,c}$ ($\sum_b \alpha_{b,c} = 1$), and 1-Lipschitz building blocks; optimizer \mathcal{O} ; (optional) stream loss weights ζ, ϕ, ν, κ .

- 1 **Init:** Initialize θ ; set spectral normalisation (SN) for all convs (operator norm ≤ 1); **for** $e = 1$ **to** E
- 2 **do**
- 3 **foreach** minibatch $\{(x_i, y_i)\}_{i=1}^B \sim \mathcal{D}$ **do**
- 4 // Resample internal randomness once per minibatch (HycAS execution protocol)
- 5 Resample random-projection filters for RPFAN and attention-noise masks for all streams, collect as Ω . // RS-style training noise at the input
- 6 **for** $i = 1$ **to** B **do**
- 7 Draw $\varepsilon_i \sim \mathcal{N}(0, \sigma^2 I)$; set $\tilde{x}_i \leftarrow x_i + \varepsilon_i$.
- 8 // Forward through the three streams + convex fusion (each stream ≤ 2 -Lipschitz)
- 9 Compute per-stream feature maps $G_b(\tilde{x}_i; \Omega)$ for $b \in \{\text{SNCAN}, \text{RPFAN}, \text{FDPAN}\}$. Fuse per channel: $z(\tilde{x}_i) \Leftarrow c \leftarrow \sum_b \alpha_{b,c} G_b(\tilde{x}_i; \Omega) \Leftarrow c$. // Loss: single fused CE, or the HycAS-weighted multi-branch objective
- 10 $L \leftarrow \kappa \mathcal{L}(z(\tilde{x}_i), y_i) + \zeta \mathcal{L}(G_{\text{FDPAN}}, y_i) + \phi \mathcal{L}(G_{\text{SNCAN}}, y_i) + \nu \mathcal{L}(G_{\text{RPFAN}}, y_i)$. Update $\theta \leftarrow \mathcal{O}(\theta, \nabla_{\theta} \frac{1}{B} \sum_i L)$. // Keep layer-wise operator norms ≤ 1 (SN) to maintain global ≤ 2 -Lipschitz envelope
- 11 Re-apply SN to all conv kernels.
- 12 // Final global calibrator (gain) to cap the network Lipschitz constant by 2
- 13 Estimate L_{net} (product of per-block bounds); scale last linear by $\gamma \leftarrow \min(1, 2/L_{\text{net}})$.

Algorithm 2 HyCAS Inference and Certification

Input: Trained HyCAS-integrated classifier f_θ (globally ≤ 2 -Lipschitz); test point x ; class set \mathcal{Y} of size K ; Gaussian noise level σ ; pilot n_0 and budget n for RS; significance α (set $\alpha_{\text{RS}} = \alpha_{\text{Lip}} = \alpha/2$).

Output: Certified label \hat{y} and radius $R > 0$, or ABSTAIN.

```

10 (A) RS branch (standard randomized smoothing). // Cohen-style certificate;
    pilot then CI
11 for  $i = 1$  to  $n_0$  do
12   Draw  $\varepsilon \sim \mathcal{N}(0, \sigma^2 I)$  and internal randomness  $\Omega$ ;  $c_i \leftarrow f_\theta(x + \varepsilon; \Omega)$ ;
13 Let  $\hat{c}_A \leftarrow \arg \max_{c \in \mathcal{Y}} \text{count}_{n_0}(c)$ . for  $i = 1$  to  $n$  do
14   Draw  $\varepsilon \sim \mathcal{N}(0, \sigma^2 I)$  and  $\Omega$ ;  $c_i \leftarrow f_\theta(x + \varepsilon; \Omega)$ ;
15 Let  $m \leftarrow \text{count}_n(\hat{c}_A)$  and  $\hat{p}_A^{\text{LB}} \leftarrow \text{CLOPPERPEARSONLOWER}(m, n, 1 - \alpha_{\text{RS}})$ . if  $\hat{p}_A^{\text{LB}} \leq \frac{1}{2}$  then
    set  $R_{\text{RS}} \leftarrow 0$ 
16 else  $R_{\text{RS}} \leftarrow \sigma \Phi^{-1}(\hat{p}_A^{\text{LB}})$ ;  $\hat{y}_{\text{RS}} \leftarrow \hat{c}_A$ .
    //  $\Phi^{-1}$  is the standard normal inverse CDF
17 (B) Lipschitz-margin branch (deterministic certificate). // HyCAS margin
    certificate
18 Freeze internal randomness  $\Omega^*$  (fix seeds), and compute logits  $s(\cdot; \Omega^*)$ .  $\hat{y}_{\text{Lip}} \leftarrow$ 
     $\arg \max_{c \in \mathcal{Y}} s_c(x; \Omega^*)$ ;  $s^{(1)} \leftarrow \max_c s_c(x; \Omega^*)$ ;  $s^{(2)} \leftarrow \max_{c \neq \hat{y}_{\text{Lip}}} s_c(x; \Omega^*)$ . if  $s^{(1)} \leq s^{(2)}$ 
    then set  $R_{\text{Lip}} \leftarrow 0$ 
19 else  $R_{\text{Lip}} \leftarrow \frac{s^{(1)} - s^{(2)}}{4}$ 
    // Since  $\text{Lip}(f_\theta) \leq 2$ , radius is (margin)/(2 · Lip)
20 (C) Pick the stronger valid certificate. if  $\max(R_{\text{RS}}, R_{\text{Lip}}) = 0$  then return ABSTAIN
21 else if  $R_{\text{RS}} \geq R_{\text{Lip}}$  then return  $(\hat{y}_{\text{RS}}, R_{\text{RS}})$ 
22 else return  $(\hat{y}_{\text{Lip}}, R_{\text{Lip}})$ 

```

A.7.2 HYCAS INFERENCE-TIME CERTIFICATION

At test time we provide two *independent* certificates, both for the exact network we evaluate:

1. **RS certificate.** We certify the smoothed classifier

$$g_\sigma(x) \triangleq \arg \max_{c \in \mathcal{Y}} \mathbb{P}_{\varepsilon, \Omega}[f_\theta(x + \varepsilon; \Omega) = c].$$

We follow the standard two-stage Monte-Carlo protocol: draw n_0 samples to select the candidate class \hat{c} and then n samples to bound its probability. Let \hat{p}_A and \hat{p}_B be the empirical proportions of the top and runner-up classes. Using exact Clopper–Pearson intervals we obtain a $(1 - \alpha)$ lower bound p_A^{LB} on the top class and an upper bound p_B^{UB} on the second. If $p_A^{\text{LB}} \leq \frac{1}{2}$ we abstain; otherwise the certified ℓ_2 radius is

$$r_2^{\text{RS}}(x) = \frac{\sigma}{2} \left(\Phi^{-1}(p_A^{\text{LB}}) - \Phi^{-1}(p_B^{\text{UB}}) \right),$$

where Φ^{-1} is the standard normal quantile. This is the tight Cohen–Rosenfeld–Kolter bound specialized and re-derived in ARS (via f -DP). In our experiments we mirror DRS sampling defaults ($n_0 = 100$, $n = 10^5$, $\alpha = 10^{-3}$). When the DRS path is enabled, class probabilities are estimated branch-wise and fused as in DRS before applying the same formula.

2. **Deterministic Lipschitz (margin) certificate.** Independently of input noise, we certify the *backbone + internal randomness* by averaging logits only over Ω :

$$Z(x) \triangleq \mathbb{E}_\Omega[s(x; \Omega)], \quad \text{with } \text{Lip}(Z) \leq 2.$$

Let $\Delta Z(x) = Z_{(1)}(x) - Z_{(2)}(x)$ be the gap between the top-two expected logits. Then for every perturbation $\|\delta\|_2 < \Delta Z(x)/4$, the $\arg \max$ of $Z(\cdot)$ is invariant; i.e., the model’s prediction is certifiably robust within radius

$$r_2^{\text{Lip}}(x) = \frac{\Delta Z(x)}{4}, \quad r_\infty^{\text{Lip}}(x) = \frac{r_2^{\text{Lip}}(x)}{\sqrt{d}}.$$

We estimate Z via Monte-Carlo over Ω (no input noise), exactly as recommended in HyCAS.

Algorithm 2 implements both procedures. In reporting, we return *two* radii $(r_2^{\text{RS}}(x), r_2^{\text{Lip}}(x))$ for the same input x . Both are valid and interpretable: the first certifies the RS/DRS-smoothed classifier, the second certifies the *Lipschitz hybrid backbone averaged over internal noise*. This mirrors the practice in ARS/RS (majority-vote certificate) and HyCAS (margin certificate) while respecting their assumptions.

A.8 EXTENDED EVALUATION SETUP

Network Execution. At the start of every mini-batch we resample, for each forward pass, (i) the attention-noise M_ω for {FDPAN, SNCAN, RPFAN} and (ii) the random projection filters for RPFAN. These samples stay fixed while adversarial examples are generated. At inference stage, for each test image, we draw one fresh set (ψ, ω) , and evaluate HyCAS against adversarial attacks to ensure adversarial robustness.

Implementation details. Following (Cohen et al., 2019; Lyu et al., 2024; Xia et al., 2024), we use ResNet-110 (He et al., 2016) on CIFAR-10/100 and ResNet-50 on remaining imaging datasets (e.g., ImageNet (Deng et al., 2009), CelebA (Liu et al., 2015)), NCT-CRC-HE-100K (Kather et al., 2018) etc.), as base classifiers for all training strategies. We report the best performance separately for a more comprehensive and fair comparison. We evaluate on CIFAR-10/100, ImageNet-1k, CelebA (unaligned, cropped attribute), NCT-CRC-HE-100K, NIH CXR, EyePACS, and HAM10000.

For Certified Defense. HyCAS certifies via a margin bound under an *at-most* 2-Lipschitz network. Let $Z(x) = \mathbb{E}_\omega[z(x)]$ denote the classifier averaged over the model’s internal randomness; since $\text{Lip}(Z) \leq 2$, a pointwise certificate is $r(x) = \frac{\Delta z(x)}{4}$, $\Delta_Z(x) = Z_{(1)}(x) - Z_{(2)}(x)$. To estimate $Z(x)$ we Monte Carlo sample only the model’s *internal* noise at inference. Unless noted otherwise, we take a pilot of $n_0 = 100$ samples to select the top class, then draw $n = 100,000$ additional samples to form one-sided confidence bounds and report $r_{\text{LCB}}(x) = \frac{\text{LCB}(Z_{(1)}(x)) - \text{UCB}(Z_{(2)}(x))}{4}$ at confidence $1 - \alpha$ with $\alpha = 0.001$. During inference we draw a fresh ω on each forward pass. To control runtime for Monte Carlo estimation, we use a fixed rule per dataset:

- CIFAR-10: certify every 5th test image (default settings $n_0=100, n=100,000, \alpha=0.001$).
- ImageNet-1k: certify every 100th test image (default settings $n_0=100, n=100,000, \alpha=0.001$).
- CelebA (ARS-style): certify a *uniform, label-stratified* subset of 200 test images using $n_0=100, n=50,000$, and failure probability 0.05 (i.e., 95% confidence).
- NCT-CRC-HE-100K, NIH ChestX-ray14, EyePACS: certify a *uniform, label-stratified* subsample per dataset sized to yield $\approx 2,000$ certified examples each (default settings $n_0=100, n=100,000, \alpha=0.001$; exact counts in the appendix).
- HAM10: certify the full test split when feasible; otherwise a uniform, label-stratified subsample (default settings $n_0=100, n=100,000, \alpha=0.001$; exact count in the appendix).

We sweep $\sigma \in \{0.25, 0.50, 1.0\}$ for comparability across settings.

For Empirical Defense. We follow the protocol of SOTA adversarial training strategy (Rice et al., 2020) to set up our experiments on our diverse datasets. For Adversarial Evaluation—HyCAS is tested under white-box attacks—PGD (Madry et al., 2018), APGD (Croce & Hein, 2020), and AutoAttack (AA) (Croce & Hein, 2020) using $\epsilon = \left\{ \frac{8}{255}, \frac{16}{255} \right\}$, step size $\alpha = \frac{20}{255}$, and 10–100 iterations.

Training Details for Certified Robustness. Following ARS, we use a single recipe per dataset and train all HyCAS-integrated backbones. Inputs are perturbed *during training only* with i.i.d. Gaussian noise $\mathcal{N}(0, \sigma^2)$ (the same σ as at certification). For CIFAR-10, we train for 200 epochs with a batch size of 256 using AdamW as the optimizer with learning rate 10^{-2} and weight decay 10^{-4} . A step scheduler is used with step size 30 and decay factor $\gamma = 0.1$. For CelebA, NCT-CRC-HE-100K, NIH CXR, EyePACS, and HAM10000, we train for 200 epochs with a batch size of 64 using SGD as the optimizer with learning rate 5×10^{-2} . A step scheduler is used with step size 3 and decay factor $\gamma = 0.8$. For ImageNet-1k, we train for 200 epochs

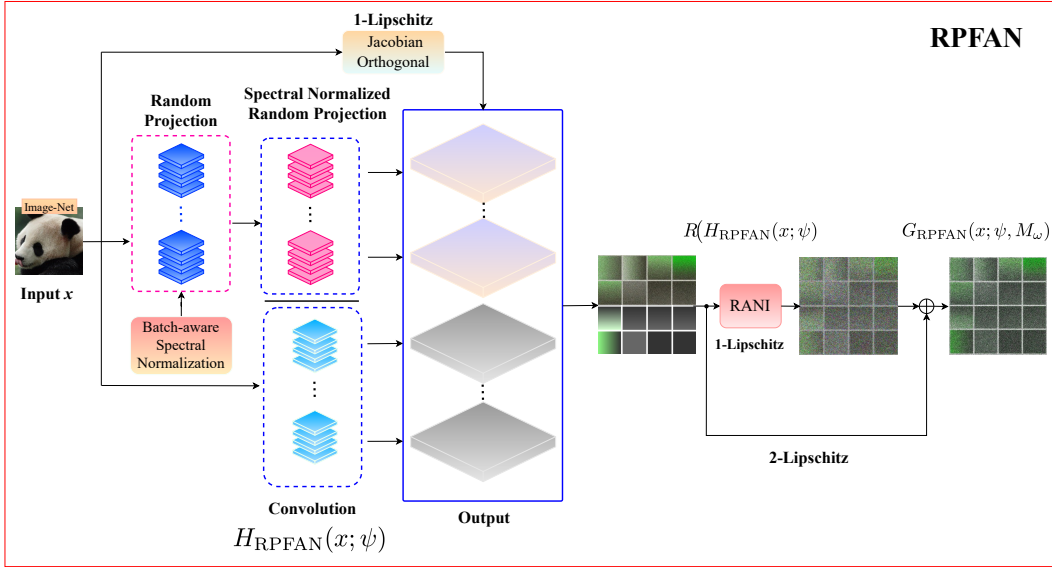


Figure 7: Overview of RPFAN stream. (i) Orthogonal 1×1 pre-mix (1-Lipschitz). (ii) Batch-aware spectral normalization of a random-projection convolution (1-Lipschitz core). (iii) RANI residual, yielding a ≤ 2 -Lipschitz stochastic block.

Table 6: Robust accuracy (%) against ℓ_∞ attacks (PGD-20 and AA-20) on NIH-CXR (left) and NCT-CRC-HE-100K (right) at $\epsilon \in \{8/255, 16/255\}$.

Method	NIH-CXR						NCT-CRC-HE-100K					
	Clean	PGD-20		AA-20		Clean	PGD-20		AA-20			
		8/255	16/255	8/255	16/255		8/255	16/255	8/255	16/255		
AT	89.1 ± 1.91	78.3 ± 2.82	68.4 ± 3.62	74.2 ± 2.93	64.1 ± 3.70	92.2 ± 1.82	80.4 ± 2.72	70.8 ± 3.52	76.3 ± 2.83	66.2 ± 3.61		
RPF	88.4 ± 1.82	84.6 ± 2.62	73.2 ± 3.42	82.5 ± 2.71	70.8 ± 3.52	91.1 ± 1.71	87.5 ± 2.51	76.6 ± 3.33	84.2 ± 2.62	72.4 ± 3.41		
CTRW	88.4 ± 1.73	85.7 ± 2.41	74.4 ± 3.22	84.5 ± 2.48	72.6 ± 3.41	90.4 ± 1.62	89.6 ± 2.33	77.5 ± 3.12	86.7 ± 2.44	75.2 ± 3.22		
DCS	87.2 ± 2.05	83.5 ± 2.65	72.3 ± 3.30	81.7 ± 2.72	69.6 ± 3.45	90.3 ± 1.93	86.5 ± 2.62	75.2 ± 3.35	83.3 ± 2.74	71.6 ± 3.46		
ARS	84.8 ± 2.22	77.2 ± 2.95	66.5 ± 3.62	72.8 ± 3.11	62.8 ± 3.72	86.8 ± 2.14	78.9 ± 2.92	68.3 ± 3.61	74.6 ± 3.11	64.5 ± 3.73		
DRS	83.9 ± 2.33	76.2 ± 2.84	65.8 ± 3.74	71.6 ± 3.12	61.9 ± 3.81	85.9 ± 2.25	77.5 ± 2.82	67.6 ± 3.82	73.5 ± 3.21	63.7 ± 3.94		
HyCAS	89.5 ± 1.64	88.6 ± 2.33	77.3 ± 3.14	86.9 ± 2.42	74.4 ± 3.33	91.3 ± 2.63	90.4 ± 2.82	79.3 ± 3.52	88.2 ± 2.63	76.7 ± 3.34		

(10+90 warm-up and main training), with a batch size of 300 using SGD as the optimizer with learning rate 10^{-1} , momentum 0.9, and weight decay 10^{-4} . A step scheduler is used with step size 30 and decay factor $\gamma = 0.1$. HyCAS injects *internal* spatial and channel attention noise on each forward pass; convolutions are regularized with spectral scaling (via FFT or power iteration) combined with GroupSort activations and convex residual gating, ensuring the network remains at most 2-Lipschitz. We optimize using categorical cross-entropy loss and report top-1 accuracy.

Adversarial Training with HyCAS for Empirical Robustness. Let $f_\theta : \mathbb{R}^d \rightarrow \mathbb{R}^C$ be the HyCAS-integrated base classifier with parameters θ , mapping an input x to its logits $f_\theta(x)$. For a given clean sample (x, y) and perturbation budget ϵ , an adversarial example x^* is obtained by maximizing the loss inside the ϵ -ball around x :

$$x^* = \arg \max_{x^* : \|x^* - x\| \leq \epsilon} \mathcal{L}_{\text{HyCAS}}(f_\theta(x^*; \Omega[A]), y), \tag{21}$$

where $\mathcal{L}_{\text{HyCAS}}$ is the task loss and $\Omega[A]$ emphasizes that gradients are taken in the *attack* phase.

Adversarial training then solves the following classical min-max problem:

$$\min_{\theta[I]} \max_{x^* : \|x^* - x\| \leq \epsilon} \mathcal{L}_{\text{HyCAS}}(f_\theta(x^*; \Omega[A]), y), \tag{22}$$

where $\theta[I]$ denotes the parameters updated during the *inference* phase.

As detailed in Algorithm 3, combining this min-max optimization with all integrated streams enables HyCAS to maintain strong adversarial resilience at inference time.

Table 7: Robust accuracy (%) against ℓ_∞ attacks (PGD-20 and AA-20) on HAM10000 (left) and EyePACS (right) at $\epsilon \in \{8/255, 16/255\}$.

Method	HAM10000					EyePACS				
	Clean	PGD-20		AA-20		Clean	PGD-20		AA-20	
		8/255	16/255	8/255	16/255		8/255	16/255	8/255	16/255
AT	75.2 ± 2.94	58.3 ± 3.81	48.4 ± 3.75	54.2 ± 3.93	44.2 ± 3.80	78.2 ± 2.91	62.4 ± 2.72	52.8 ± 3.52	58.3 ± 2.83	48.2 ± 3.61
RPF	74.3 ± 2.86	64.6 ± 3.62	53.3 ± 3.52	62.6 ± 3.71	50.4 ± 3.58	77.1 ± 2.90	68.5 ± 2.61	57.6 ± 3.53	66.4 ± 2.73	54.4 ± 3.44
CTRW	74.3 ± 2.75	64.7 ± 3.42	54.2 ± 3.43	63.3 ± 3.48	51.2 ± 3.52	76.4 ± 2.84	70.1 ± 2.53	58.5 ± 3.43	69.7 ± 2.64	56.1 ± 3.31
DCS	73.2 ± 2.94	63.5 ± 3.65	52.4 ± 3.30	61.4 ± 3.72	49.5 ± 3.45	76.4 ± 2.94	67.5 ± 2.62	56.2 ± 3.35	65.3 ± 2.74	53.6 ± 3.46
ARS	69.8 ± 3.22	56.2 ± 3.95	46.5 ± 3.62	52.7 ± 4.10	42.8 ± 3.71	72.9 ± 3.97	61.9 ± 2.91	50.3 ± 3.61	57.6 ± 2.94	46.5 ± 3.73
DRS	68.9 ± 3.28	55.3 ± 3.84	45.7 ± 3.75	51.6 ± 4.12	41.8 ± 3.81	71.9 ± 3.86	60.5 ± 2.81	49.6 ± 3.82	56.5 ± 2.92	45.7 ± 3.94
HyCAS	74.6 ± 2.74	67.8 ± 3.43	55.3 ± 3.14	65.8 ± 3.42	53.1 ± 3.33	77.6 ± 2.79	72.6 ± 2.72	60.5 ± 3.43	71.8 ± 2.82	58.3 ± 3.32

Table 8: RS/DRS vs HyCAS certified accuracy on EyePACS NCT-CRC-HE-100K benchmarks. The best performance under each training strategy is **bold**.

Approach	σ	EyePACS					NCT-CRC-HE-100K				
		ℓ_2 radius r (%)					ℓ_2 radius r (%)				
		0.00	0.25	0.50	0.75	1.00	0.00	0.25	0.50	0.75	1.00
DRS	0.25	81.3 ± 1.92	60.1 ± 2.83	50.1 ± 1.53	40.9 ± 2.04	26.2 ± 2.69	89.5 ± 2.78	67.6 ± 2.63	56.7 ± 3.35	45.3 ± 2.27	30.5 ± 3.54
	0.5	78.9 ± 0.91	57.7 ± 2.82	51.8 ± 1.34	42.1 ± 0.96	30.4 ± 3.74	85.2 ± 1.67	65.6 ± 1.89	56.2 ± 1.23	48.2 ± 1.67	33.1 ± 1.20
ARS	0.25	83.1 ± 1.35	62.9 ± 2.93	47.9 ± 1.94	40.7 ± 2.32	36.2 ± 3.73	91.7 ± 1.84	69.3 ± 2.07	59.4 ± 2.37	48.3 ± 3.91	31.9 ± 2.63
	0.5	80.9 ± 1.14	60.7 ± 2.27	51.5 ± 1.42	42.2 ± 2.68	37.5 ± 0.98	87.8 ± 2.25	68.4 ± 1.91	60.1 ± 1.01	50.7 ± 0.53	34.2 ± 1.39
HyCAS	0.25	86.7 ± 0.97	66.1 ± 1.62	51.4 ± 2.74	45.7 ± 1.27	39.2 ± 2.61	95.4 ± 2.02	72.9 ± 1.63	63.1 ± 1.59	51.7 ± 3.11	33.2 ± 1.84
	0.5	82.6 ± 1.89	63.9 ± 1.74	53.2 ± 2.81	46.3 ± 1.45	41.5 ± 1.67	92.3 ± 0.61	71.7 ± 1.11	63.4 ± 1.36	52.2 ± 1.21	36.9 ± 2.57

Algorithm 3: Adversarial Training with HyCAS

- 1: **Require:** HyCAS integrated base classifier $\{\theta(\cdot)\}$ with learning parameter θ ; Perturbation size ϵ ; Attack step size a ; Number of attack iterations k ; Training set $\{x, y\}$; Generated attention noise M_ω by RANI module.
- 2: **Procedure:**
- 3: **while** not converged **do**
- 4: Sample a batch $\{bx, by\}_{i=1}^n$ from $\{x, y\}$;
- 5: **Apply HyCAS for Attack phase:**

$$z(x)_{:,c} = \sum_{b \in \mathcal{B}} \alpha_{b,c} [G_b(x; \Omega)]_{:,c} + R \left(\sum_{b \in \mathcal{B}} \alpha_{b,c} [G_b(x; \Omega)]_{:,c}; M_\omega \right); \quad c = 1, \dots, C.$$

- 6: Compute the HyCAS-integrated network is optimised with a standard ℓ_∞ loss:

$$\mathcal{L}_{HyCAS} = \zeta \odot \mathcal{L}_{FD PAN} + \varphi \odot \mathcal{L}_{SNCAN} + \nu \odot \mathcal{L}_{RPFAN} + \kappa \odot \mathcal{L}_{RANI}$$

$$\min_{\theta} \max_{x^*} (\mathcal{L}_{HyCAS}(\{\theta(x^*; \Omega[A]), y\})) \quad \text{s.t. } \|x^* - x\| \leq \epsilon$$

- 7: **Generate Adversarial Examples:**
- 8: Randomly initialize adversarial perturbation δ ;
- 9: **for** $i = 1$ to k **do**

$$\delta \leftarrow \delta + a \cdot \text{sign}(\nabla_{bx} \mathcal{L}_{HyCAS}(\{\theta(bx^*; \Omega), by\})) \quad bx^* \leftarrow \text{Clip}_{bx}^\epsilon(bx + \delta)$$

- 10: **end for**
- 11: **Apply HyCAS for Inference phase:**

$$z(x)_{:,c} = \sum_{b \in \mathcal{B}} \alpha_{b,c} [G_b(x; \Omega)]_{:,c} + R \left(\sum_{b \in \mathcal{B}} \alpha_{b,c} [G_b(x; \Omega)]_{:,c}; M_\omega \right); \quad c = 1, \dots, C.$$

$$\min_{\theta} \max_{x^*} (\mathcal{L}_{HyCAS}(\{\theta(x^*; \Omega[A]), y\})) \quad \text{s.t. } \|x^* - x\| \leq \epsilon$$

- 12: **Adversarial Training Optimization:**

$$\theta = \theta - \nabla_{\theta} (\mathcal{L}_{HyCAS}(\{\theta(x^*, \Omega), y\}))$$

- 13: **end while**

Table 9: Computational cost comparison between vanilla backbones and their HyCAS-integrated counterparts. We report the number of parameters (M), FLOPs (G), activation memory (MB), and inference time (ms) for ResNet-110 on CIFAR-10 ($32 \times 32 \times 3$) and ResNet-50 on ImageNet-1K ($224 \times 224 \times 3$).

Backbone	Variant	Inputs	Parameters (M)	FLOPs (G)	Memory (MB)	Inference Time (ms)
ResNet-110	Vanilla	$32 \times 32 \times 3$	27.6	8.10	105.33	0.33
	HyCAS		57.8	126.5	220.5	5.14
ResNet-50	Vanilla	$224 \times 224 \times 3$	23.3	113.8	88.89	4.62
	HyCAS		102.7	1682.5	391.9	68.3

A.9 ADDITIONAL EXPERIMENTAL RESULTS

Empirical robustness on Chest Xray, Histopathology, Dermoscopy, Funduscopy modalities.

Across our empirical evaluations (Tables 6–7), HyCAS achieves the highest robust top-1 accuracy under PGD-20 and AA-20 at $\epsilon \in \{8, 16\}/255$. Specifically, on the NIH-CXR benchmark, HyCAS retains robust accuracy, outperforming the leading baseline (CTRW) by up to **+1.0–2.2%** while competitive clean-set accuracy (89.5% vs. 89.1%) vs. AT. A similar trend appears on the NCT-CRC-HE-100K dataset, where HyCAS records robust accuracies of **76.7–79.3%** against the same attacks, edging past CTRW by $\approx +1\%$ and leaving earlier certified defences (e.g., ARS, DRS) more than **+7%** behind at the larger perturbation strength. Dermoscopic HAM10000 and fundus-image EyePACS exhibit the same hierarchy: HyCAS secures robust accuracies of **53.1–67.8%** against PGD-20 and AA-20 attacks on HAM10000—roughly **+1.1–7.4%** better than the next-best adversarial defence—and widens the margin on EyePACS to **58.3–72.6%**, thereby surpassing the leading baseline CTRW by **+2.0–3.3%**. *Together, these results show that HyCAS transfers its randomized Lipschitz-based strategy from certified to empirical settings, preserving clean accuracy while preserving adversarial robustness against strong first-order attacks.*

Evaluation under stronger PGD attacks on other vision benchmarks (Figs. 8–9) reveals that HyCAS not only wins at standard PGD-20 settings (App. A.8) but also sustains its lead as the adversary grows stronger. When the perturbation strength is swept from $\epsilon = 0.01 \rightarrow 0.08$ on CIFAR-10, HyCAS traces the upper envelope of robust-accuracy curves, preserving a $\approx 10\%$ gap at the maximum perturbation strength, where all baselines collapse sharply. An analogous pattern emerges on CIFAR-100 as the number of PGD iterations climbs from **10** \rightarrow **100**: while every defense degrades monotonically, HyCAS declines more gracefully and ends **7–12%** above the closest competitor at 100 steps, confirming that its internally resampled attention noise and random projections thwart extended optimization. Thus, *this randomized, Lipschitz-constrained design* scales gracefully with both perturbation size and steps, offering adversarial robustness and a broader safety margin.

Certified adversarial robustness on EyePacs and NCT-CRC-HE-100K. Across the complete set of baselines in Table 8, HyCAS delivers the strongest certified accuracy for every inspected radius-noise pair. On the EyePacs benchmark, at the representative medium radius $r=0.75$ it reaches **45.7%** certified accuracy for $\sigma = 0.25$ and **46.3%** for $\sigma = 0.50$, outpacing the best competing method (DRS/ARS) by 4.1–4.8%. Even in the large-radius tail ($r=1.0$), HyCAS maintains **39.2%** ($\sigma = 0.25$) and **41.5%** ($\sigma = 0.50$), widening the gap over the strongest baseline by up to 4.0%.

A comparable pattern emerges on the NCT-CRC-HE-100K histopathology dataset. At $r=0.75$, HyCAS secures **51.7%** ($\sigma = 0.25$) and **52.2%** ($\sigma = 0.50$), improving on the best baseline by 1.5–3.4%. In the challenging $r=1.0$ regime it still records **33.2%** ($\sigma = 0.25$) and **36.9%** ($\sigma = 0.50$), extending the lead to as much as 2.7%.

Besides robustness, HyCAS achieves the highest clean accuracy on both datasets—**86.7%** on EyePacs and **95.4%** on NCT-CRC-HE-100K for $\sigma = 0.25$ —underscoring that its certified gains do not come at the expense of nominal performance.

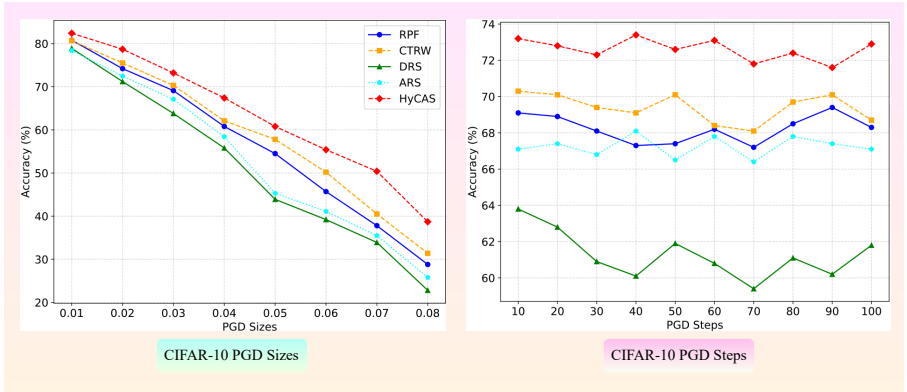


Figure 8: Empirical robustness of HyCAS versus leading baselines (RPF, CTRW, DRS, ARS) on CIFAR-10 under strong PGD attacks. We evaluate two settings: (1) perturbation sizes ϵ from 0.01 to 0.08 and (2) iteration steps from 10 to 100.

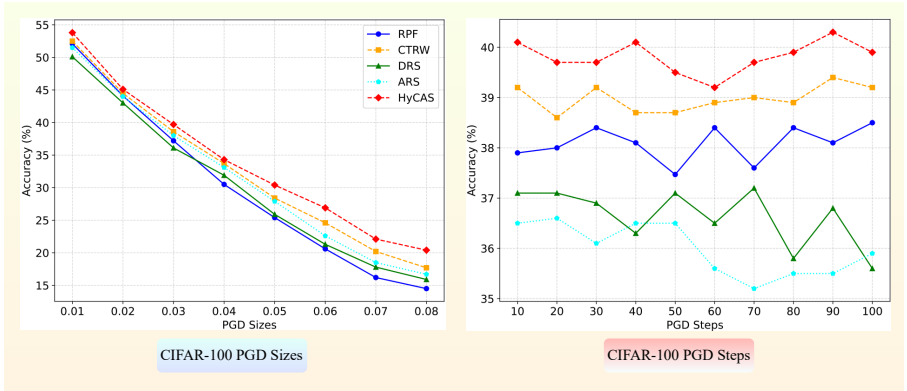


Figure 9: Empirical robustness of HyCAS versus leading baselines (RPF, CTRW, DRS, ARS) on CIFAR-100 under strong PGD attacks. We evaluate two settings: (1) perturbation sizes ϵ from 0.01 to 0.08 and (2) iteration steps from 10 to 100.

Computational cost analysis. Table 9 quantifies the computational overhead of integrating HyCAS into standard CNN backbones. On CIFAR-10 with ResNet-110, replacing the vanilla backbone with its HyCAS counterpart roughly doubles the parameter count and activation memory (27.6M \rightarrow 57.8M and 105.33MB \rightarrow 220.5MB, i.e., $\approx 2.1\times$ in both cases). In contrast, FLOPs and inference time increase by about an order of magnitude: 8.10G \rightarrow 126.5G FLOPs and 0.33ms \rightarrow 5.14ms i.e., $\approx 15.6\times$. A similar pattern is observed on ImageNet-1K with ResNet-50, where HyCAS induces a 4.4 \times increase in parameters and memory (23.3M \rightarrow 102.7M and 88.89MB \rightarrow 391.9MB), while FLOPs and inference time grow by $\approx 14.8\times$ (113.8G \rightarrow 1682.5G and 4.62ms \rightarrow 68.3ms).

To better localize this overhead, we also compare HyCAS with a single intermediate 3×3 convolutional block of 256 channels in ResNet-110. Substituting this standard convolution with a HyCAS block increases the number of parameters by 5.09 \times , whereas the corresponding FLOPs rise by 14.05 \times , indicating that most of the extra cost stems from repeated stochastic operations rather than weight storage. These block-level ratios are consistent with the backbone-level trends above, where HyCAS trades only $\approx 2\text{--}4\times$ more parameters and memory for roughly a $\approx 15\times$ increase in arithmetic and runtime.

Overall, HyCAS is best characterized as a parameter-moderate but compute-heavy defense: the three Lipschitz-constrained stochastic streams (FDPAN, SNCAN, and RPFAN) together with the

RANI module primarily inflates FLOPs and inference time, while absolute inference times remain in a practical range (a few milliseconds on CIFAR-10 and tens of milliseconds on ImageNet per image on an A100-class GPU). In return, HyCAS consistently delivers state-of-the-art certified and empirical robustness across CIFAR-10, ImageNet, and the medical-imaging benchmarks reported in Tables 1–4 and 6–8, making this overhead acceptable for many offline or near real-time deployment scenarios.

A.10 ABLATION STUDY

Table 10 traces a controlled progression from the regularized-smoothing (RS) baseline to the full HyCAS model, revealing how each block incrementally strengthens robustness. Replacing ordinary convolutions with the spectrally-normalized **SNCAN** backbone already raises certified accuracy at the medium radius ($r=0.75$) from 32.4% to 36.9% and improves PGD-20 robustness by 3.7%, indicating that spectral control alone substantially smooths the gradient landscape. When the orthogonal **RPFAN** branch is introduced next, certified and empirical accuracies climb further to 40.2% and 64.8%, respectively, showing that decorrelated projections supply complementary features beyond spectral stabilization. Extending the spectrum through **FDPAN** yields another gain—42.3% certified and 66.7% empirical—confirming that high-frequency cues remain valuable even under ℓ_2 certification. Finally, injecting data-independent attention noise via **RANI** closes the gap between certified and empirical metrics, culminating in 44.3% certified accuracy and 70.1% PGD-20 robustness, which exactly matches the performance of the complete HyCAS system. Altogether, these sequential additions deliver an aggregate improvement of +11.9% certified and +12.6% empirical robustness over the RS baseline, underscoring that each module contributes a distinct yet additive benefit to adversarial defense.

Table 10: Module-wise contribution for certified and empirical adversarial robustness on CIFAR-10 benchmark. Here, we have used $\sigma = 0.50$.

Variant	Accuracy (%)	
	Certified ($r=0.75$)	PGD-20 ($\epsilon=8/255$)
RS	32.4	57.5
+ SNCAN	36.9	61.2
+ RPFAN	40.2	64.8
+ FDPAN	42.3	66.7
+ RANI	44.3	70.1

A.11 DISCUSSION

HyCAS is designed to reduce the gap between provable ℓ_2 robustness and empirical ℓ_∞ robustness by combining a globally Lipschitz design with carefully structured internal stochasticity. This section focuses on why this design yields strong certified guarantees and how it simultaneously improves empirical robustness across natural and medical imaging benchmarks.³

Certified robustness from a randomized Lipschitz network. The certified guarantee provided by HyCAS is margin-based: if

$$Z(x) = \mathbb{E}_\Omega[s_\theta(x; \Omega)], \quad \Delta Z(x) = Z_{(1)}(x) - Z_{(2)}(x),$$

denote respectively the logits averaged over the internal randomness and their top-two gap, and if $\text{Lip}(Z) \leq 2$, then

$$r_2(x) = \frac{\Delta Z(x)}{4}$$

is a valid pointwise ℓ_2 certificate (Corollary 1). This guarantee acts on the *expected logits* of a globally ≤ 2 -Lipschitz network obtained by stacking HyCAS blocks, each of which combines a 1-Lipschitz deterministic core (spectrally normalized convolutions, orthogonal channel mixing, low-pass DCT, and spectrally normalized random projections) with a 2-Lipschitz attention-noise residual. The convex fusion of the three streams and the expectation over Ω preserve the global ≤ 2 -Lipschitz constant.

³See Sections 3–4 and Appendix A for full details of the architecture, certification scheme, and experimental setup.

This certificate is qualitatively different from the randomized smoothing (RS) radius of Cohen et al. based on smoothed class probabilities and Gaussian concentration. It is not a relaxed or “looser” version of the RS bound: RS certifies the majority vote of a noise-perturbed classifier, whereas HyCAS certifies the margin of a Lipschitz-constrained expected-logit map. Which radius is larger in practice therefore depends on how training shapes the *margin distribution* under each mechanism, not on a direct comparison of constants in the formulas.

Empirically, HyCAS consistently achieves higher certified accuracy than RS, IRS, DRS, ARS and deterministic Lipschitz baselines (LOT, SLL) at all reported radii on CIFAR-10/100, ImageNet and the medical datasets (Tables 1- 2, 8). For example, on CIFAR-10 at radius $r = 0.75$ and $\sigma \in \{0.25, 0.50\}$, HyCAS attains 44.3% certified accuracy, which is 5.2–18.2 points above prior methods; at $r = 2.0$ and $\sigma = 0.50$, it still retains 12.5%, exceeding the strongest baseline by 4.0–12.5 points. Similar gains appear on ImageNet, CelebA, HAM10000, NIH-CXR, EyePACS and NCT-CRC-HE-100K. These improvements cannot be explained by small fluctuations in clean accuracy alone, indicating that the architecture and training jointly enlarge $\Delta Z(x)$ for many points while respecting the conservative $\text{Lip}(Z) \leq 2$ envelope. For example, on CIFAR-10 with $\sigma = 0.25$, RS attains 75.3% smoothed clean accuracy at $r = 0$ and 26.1% certified accuracy at $r = 0.75$, whereas HyCAS reaches 85.4% at $r = 0$ and 44.3% at $r = 0.75$ (Table 1). Thus, the gain at a non-zero radius (+18.2 points at $r = 0.75$) is substantially larger than the gain at $r = 0$ (+10.1 points), indicating that HyCAS’s Lipschitz-constrained hybrid architecture enlarges robust margins around inputs rather than merely improving accuracy on unperturbed data.

The ablation in Table 10 illustrates this mechanism: starting from an RS-style baseline, replacing standard convolutions by SNCAN, then adding RPFAN, FDPAN and finally RANI, monotonically increases certified accuracy at $r = 0.75$ on CIFAR-10 from 32.4% to 44.3%. Each variant uses the same backbone, noise level and objective; the only changes are architectural. This progression shows that the larger certified radii arise from reshaping the margin distribution under a Lipschitz constraint, rather than from a fundamentally stronger analytical bound.

From a theoretical perspective, the contribution is to extend margin-based ℓ_2 certification to networks with *internal stochasticity* and to demonstrate that such networks can be trained at scale. The analysis proves that the expected logits of a HyCAS network remain ≤ 2 -Lipschitz despite random projections and stochastic attention, and that this property can be enforced layerwise (via spectral normalization and calibrated residual scaling) in standard CNN backbones while still achieving competitive clean accuracy on large benchmarks.

Mechanisms underlying empirical ℓ_∞ robustness. The same ingredients that support the certificate also improve robustness against strong ℓ_∞ attacks such as APGD, PGD and AutoAttack. Several aspects of the design are central:

- **Spectral control.** SNCAN replaces standard convolutions by spectrally normalised ones, constraining the operator norm of each kernel and smoothing the loss landscape. This reduces the ability of first-order attacks to exploit sharp directions in the input space.
- **Random projections.** RPFAN combines an orthogonal 1×1 channel pre-mix with batch-aware spectral normalisation of random projection filters. This decorrelates channels and redistributes energy while preserving local geometry, making adversarial search less aligned with a single vulnerable feature direction.
- **Frequency-aware filtering.** FDPAN uses low-pass DCT masking and orthogonal mixing to suppress brittle high-frequency content where small ℓ_∞ perturbations can hide, without discarding all high-frequency information that remains useful for classification.
- **Randomized Attention Noise Injection (RANI).** RANI injects a bounded, data-independent attention mask after each Lipschitz core and at the fused output. For each fixed noise realization, the module is 2-Lipschitz, but across evaluations it presents a shifting, yet certifiably bounded, optimisation landscape.

Combined with adversarial training (Algorithm 3), these components yield strong empirical robustness. Across all four medical benchmarks, HyCAS attains the highest robust accuracy under APGD-20 and AA-20 at $\epsilon \in \{8/255, 16/255\}$ while maintaining clean accuracy that is on par with

or slightly better than existing adversarially trained and randomized baselines (Tables 3- 4, 6- 7). On CIFAR-10/100, HyCAS dominates the robust-accuracy curves across perturbation sizes and attack steps (Figures 2- 3, 8- 9): as ϵ increases from 0.01 to 0.08 or the number of PGD/APGD iterations grows from 10 to 100, all baselines degrade sharply, whereas HyCAS declines more gradually and preserves a 7–12 point margin at the strongest settings.

Importantly, during attack generation the internal noise is held fixed per adversarial example, so gradients remain well-defined; stochasticity is only exploited across examples, not within the optimisation path. Together with the global Lipschitz control, this suggests that the improved ℓ_∞ robustness comes from genuinely harder optimisation and smoother gradients rather than from gradient masking.

The ablation in Table 10 again mirrors this: each successive module added to the RS baseline improves both certified accuracy and PGD-20 robustness on CIFAR-10 at $r = 0.75$ and $\epsilon = 8/255$, culminating in a total gain of +11.9% certified and +12.6% empirical robustness. This tight coupling supports the view that HyCAS does not trade certified and empirical robustness against each other, but instead uses a shared Lipschitz–randomized structure to improve both.

Certified–empirical trade-offs. Figure 4 summarizes HyCAS as a three-way Pareto frontier that trades clean accuracy, certified ℓ_2 accuracy at radius r , and empirical ℓ_∞ robustness at perturbation strength ϵ . The frontier is smooth and strictly decreasing: enlarging the certified radius inevitably reduces empirical robustness. Two systematic gaps appear.

First, in the small-perturbation regime, empirical ℓ_∞ robustness lies well above the certified ℓ_2 accuracy at comparable scales, reflecting the inherent pessimism of worst-case Lipschitz bounds. Many points are robust in practice beyond what a global constant can certify. Second, for large radii and perturbations, the gap widens further due to the norm mismatch: the inequality $\|\delta\|_2 \leq \sqrt{d} \|\delta\|_\infty$ is loose at image scale, so a model that is provably stable to moderate ℓ_2 perturbations can empirically withstand much stronger ℓ_∞ attacks than suggested by the ℓ_2 certificate.

Adjusting the smoothing noise σ provides a practical knob along this frontier. Increasing σ from 0.25 to 0.50 leaves performance at intermediate radii (e.g., $r = 0.75$) almost unchanged, yet substantially boosts certified accuracy in the high-radius tail: on CIFAR-10, accuracy at $r = 2.0$ increases from 8.5% to 12.5%, and on ImageNet from 5.4% to 24.8%, while small- ϵ APGD-20 robustness remains competitive. This behaviour shows that, despite the conservative constant 1/4 in the margin bound, training under a global $\text{Lip} \leq 2$ constraint can still produce margin distributions that deliver non-trivial certified radii without destroying empirical robustness.

Limitations. The theoretical guarantees in this work are derived from a global ≤ 2 Lipschitz envelope and a margin bound $r_2(x) = \Delta Z(x)/4$ on the expected logits. This certificate is based on different assumptions than randomized-smoothing bounds, which operate on smoothed class probabilities, and the two guarantees are therefore not directly ordered in terms of tightness. Our analysis does not attempt to prove that the resulting radius is universally stronger than the randomized-smoothing radius; instead, it shows that, for the randomized, Lipschitz-constrained HyCAS architecture, shaping the margin distribution under a global ≤ 2 -Lipschitz constraint yields practically useful ℓ_2 radii that empirically improve on RS-style baselines using the same backbones. The present theory is restricted to ℓ_2 perturbations, while robustness to ℓ_∞ attacks is assessed empirically, and extending the framework to tighter, norm-adaptive or direct ℓ_∞ certificates is left for future work. Finally, HyCAS is compute-heavy: integrating three stochastic streams and the RANI module into standard CNN backbones roughly doubles parameters and memory but increases FLOPs and inference time by about an order of magnitude (Table 9). Consequently, our method is most suitable for offline or near real-time scenarios where this overhead is acceptable, and designing lighter-weight HyCAS variants is an important direction for future work.